UNIVERSITA' DEGLI STUDI DI PADOVA

Dipartimento di Ingegneria Industriale DII

Corso di Laurea Magistrale in Ingegneria dei Materiali

Additive Manufacturing of Hierarchically Porous Aluminosilicate Ceramics

Relatrice: Ing. Giorgia Franchin

Correlatore: Prof. Paolo Colombo

Laureando: Marco Lorenzo D'Agostini

1156072

Anno Accademico 2018/2019

Alla mia famiglia e ai miei amici, la mia seconda famiglia

Abstract

Additive manufacturing (AM) is well suited to the production of porous components with tailored architecture. Geopolymer-zeolite composites with hierarchical porosity in the micro-, meso- and macro-scales for desiccation of natural gas streams were obtained through robocasting of spanning beam lattices and extensively characterised through diffractometry, compression testing, microscopy and N_2 adsorption. The composites present a substantially increased specific surface area compared to the unfilled matrix and the zeolites were shown to have good water adsorption potential. The use of 3D-printed monoliths is attractive compared to conventional granular zeolite beds due to their superior permeability and easier handling.

Contents

Chapter 1

Additive Manufacturing

Additive Manufacturing (AM) is an umbrella term for a number of manufacturing techniques where objects are formed through the successive addition of layers of material on top of each other following a computer-generated model. This approach is opposed to conventional ”subtractive” methods such as machining and casting where objects are formed and then shaped through progressive removal of material by dies or cutting tools. The advantages of AM reside in the ability to produce a variety of complex geometries with minimal material waste and considerable design flexibility without requiring the use of geometry-specific tools, however its large-scale use in industry is still precluded by high costs and time consumption compared to more traditional techniques.[26]

One of the first AM techniques was stereolithography (SLA), developed in 1986, where items are formed through successive polymerisation of photocurable resins by use of UV light or electron beams (Fig. 1.1). The liquid monomers, usually acrylic or epoxy-based, are placed in a vat where the focused light beam traces the shape of the object in order to form a horizontal slice of the CAD model: once a layer is solidified, a mobile platform moves the item to coat the surface with a fresh layer of resin and the process is repeated until the final shape is obtained. Excess unreacted resin is then removed in a post-printing treatment. SLA is suitable for forming photocurable resins filled with ceramic particles, which may then be debound and sintered to obtain dense ceramic parts with complex geometries.[26] Digital Light Processing (DLP) is a variant of the process where instead of a focused beam reticulation is achieved by exposing the resin to an image generated by a projector, thus curing all points of a slice simultaneously and decreasing printing time although with some reduction in surface finish and geometrical tolerances. Santoliquido et al.[32] showed that cellular structures produced through DLP of an acrylic-alumina slurry were suitable as high-performance automotive catalytic supports and heat exchangers in industrial furnaces: the unique advantage of AM is the ability to design and manufacture foams with specific designs and geometries which are optimised for a particular application, while conventional methodologies (e.g. foaming of ceramic slurries through the use of surfactants) can only produce stochastic structures. Stereolithographic techniques can also be employed to form parts with minimum resolution in the ≈ 10 μm range and excellent geometric tolerance. Kelvin lattices with 1 mm cells for tissue engineering applications (Fig. 1.2) were successfully produced by Schmidt et al.[34] through DLP of an acrylic-glass slurry successively converted into wollastonite-diopside bioactive glass-ceramic by heat-treatment.

In Fused Deposition Modelling (FDM) a continuous filament of thermoplastic polymer (usually PLA) passes through a nozzle where it is heated to partial fusion and deposited onto the object, while the rapid solidification of the melt ensures good adhesion and a stable substrate for the overlying layers; this is the most commonly technique used by hobbyists due to the extremely low costs and rapid printing times. In powder bed techniques the item is formed by selective fusion of consecutive layers of powder through the use of an appropriate binder (such as in ink-jet printing) or a high-energy laser source: the latter technique may be applied for direct sintering of ceramic particles (Selective Laser Sintering or SLS) or fusion of metallic powders (Direct Metal Laser Sintering or DLSM).[31] DLSM was employed to manufacture the liquid injector nozzles in the Vulcain 2.1 propulsion system for ESA's Ariane 6 launcher, whose maiden flight is scheduled for 2020, allowing a substantial reduction of costs and part count compared to traditional casting and machining methods.[36]

The term "Direct Ink Writing" broadly refers to a subset of AM methodologies primarily used for the production of ceramic bodies with complex shapes through extrusion of droplet- or filament-based inks. In droplet-based techniques a liquid phase is either deposited onto a powder bed to induce coalescence of the particles (three-dimensional printing or 3DP) or used as a standalone ink which solidifies by solvent evaporation (Direct Ink-Jet Printing): a binder solution is used in the first case, and a colloidal suspension of ceramic particles in the second. These methods are useful for spanning structures with large unsupported areas, as the powder bed acts as a support surface, but often result in poor surface finish due to droplet spreading phenomena. On the other hand in filament-based techniques, which include robocasting and fused deposition (similar to FDM for polymeric materials), the ink is continuously extruded through a nozzle to produce a filament with some degree of self-support through the use of appropriate rheology or setting mechanisms.[20]

Inks used in robocasting are formulated to exhibit a rheological behaviour which can be ascribed to a Herschel-Bulkley non-Newtonian fluid. The shear motion of such a fluid can be expressed as:[8]

$$\tau = \tau_y + m\dot{\gamma}^n \tag{1.1}$$

The shear stress, τ, depends on the shear rate $\dot{\gamma}$ through a non linear relationship expressed by the parameter n; for $n < 1$ the fluid is pseudoplastic and a reduction in viscosity is observed with increasing shear rate allowing the ink to flow easily from the nozzle. Moreover, this model is characterised by the presence of a yield stress τ_y below which the fluid behaves like a solid: this feature is particularly important in robocasting as the printed structures are required to support their own weight and maintain the correct shape before any definitive setting mechanisms, such as solvent evaporation or gelation, can take place. The correct rheology is achieved through the use of an appropriate binder. For example Bai et al.,[2] whose work forms part of the basis for this project, reported the use of poly-ethylene glycol (PEG) as a binder for robocasting of geopolymeric slurries showing the potential for producing highly optimised foam architectures for thermal insulation and wastewater treatment applications. Porous ZSM-5 zeolite monoliths (Fig. 1.2.b) were produced by Couck et al.[9] through extrusion of powders in an aqueous suspension with bentonite binder; the resulting structures exhibited strong CO_2 adsorption and excellent separation potential for the CO_2/N_2 and CO_2/CH_4 systems. Finally, robocasting is a flexible technique and can be employed for a variety of complex architectures: Muth et al.[25] used a foamed alumina suspension stabilised through careful control of the Al_2O_3-H_2O contact angle to print honeycomb structures with porous struts for catalyst support applications (Fig. 1.2.c) through a novel approach termed Direct Foam Writing (DFW).

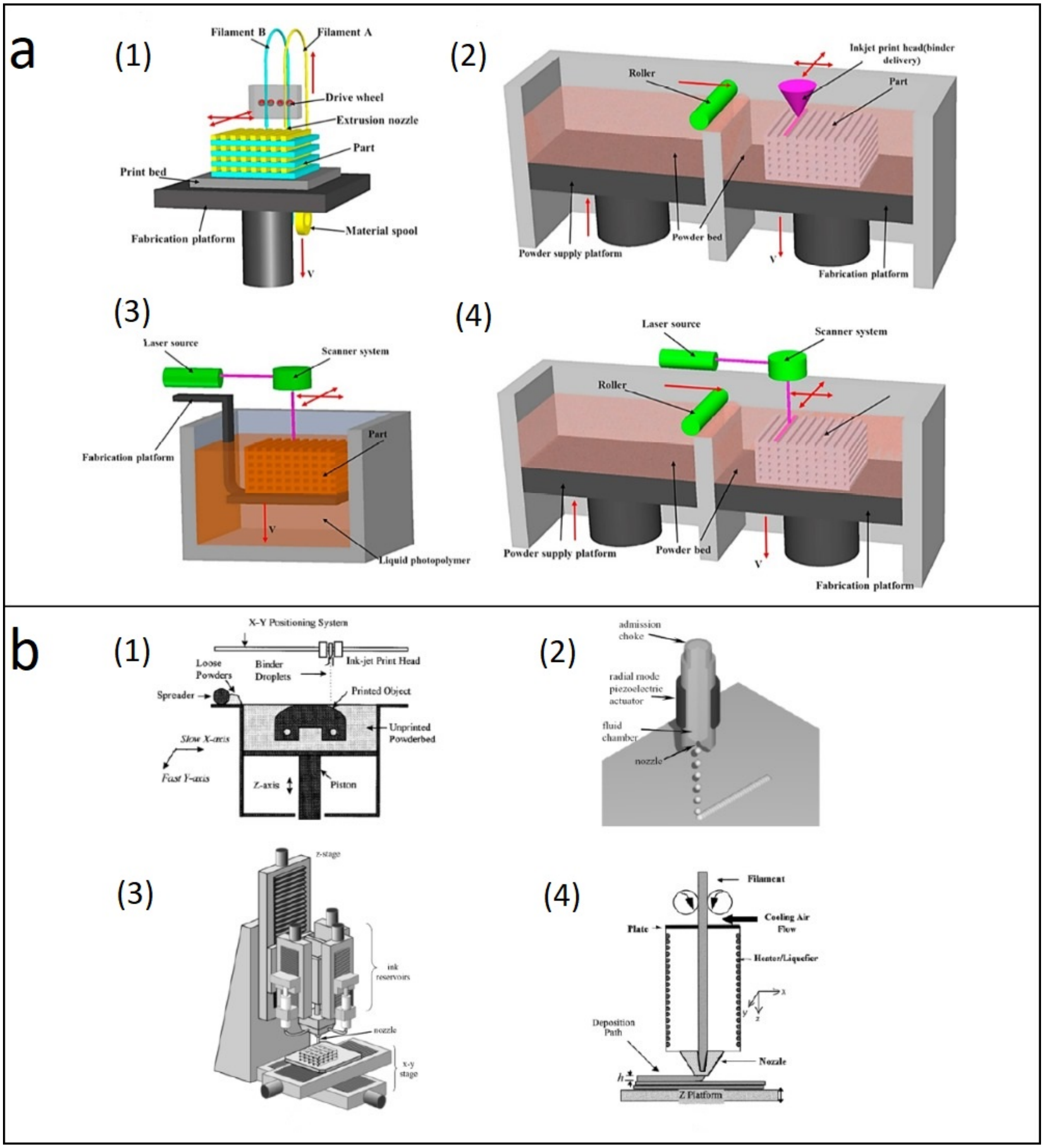

Figure 1.1: Schematic illustration of various AM techniques (a): Fused Deposition Modelling (1), Ink-Jet Printing (2), stereolitography (3) and Powder Bed Fusion (4).[26] Schematic illustration of droplet- and filament-based DIW techniques: powderbed printing (1), Direct Ink-Jet Printing (2), robocasting (3) and fused deposition of ceramics (4).[20]

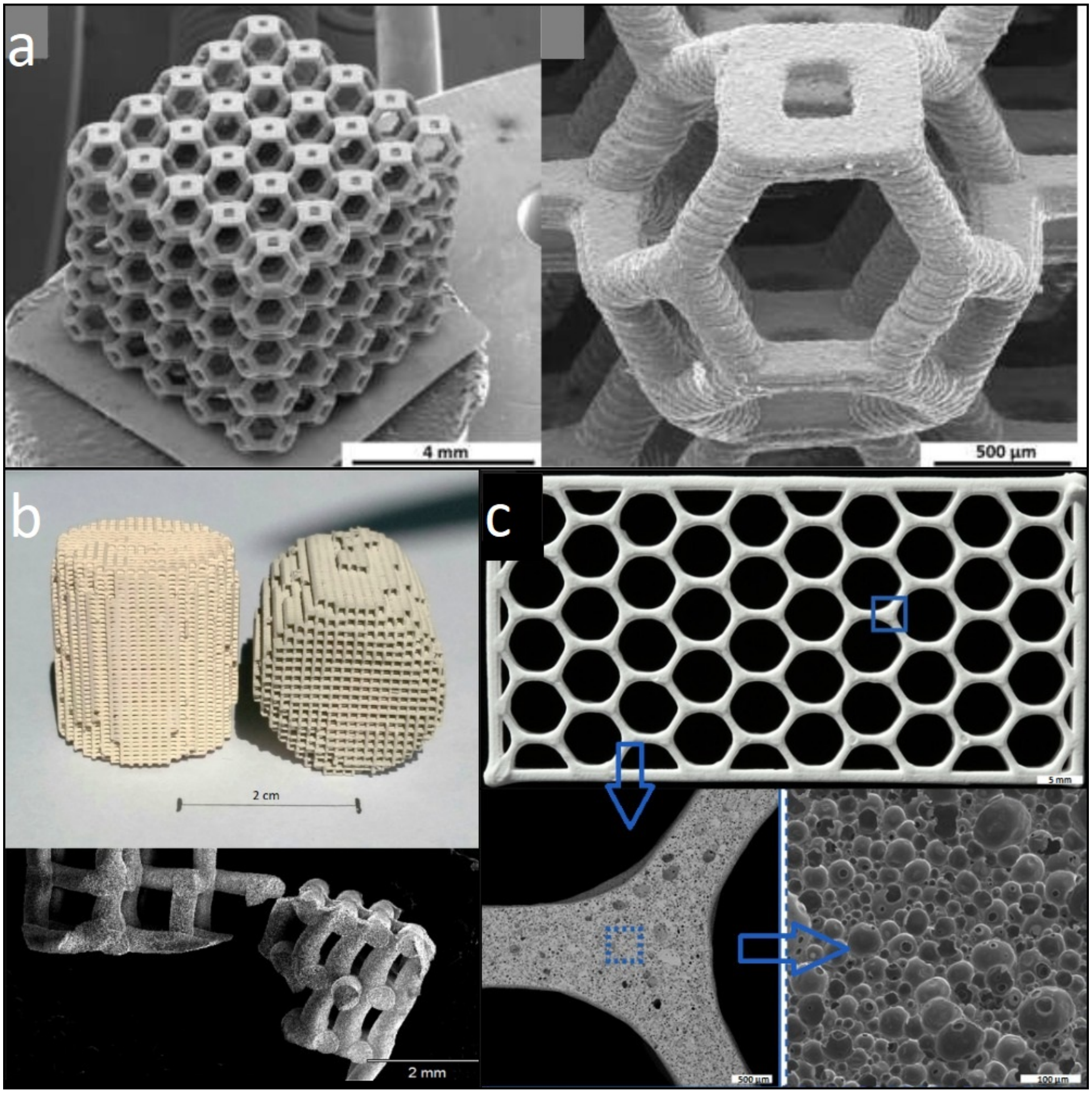

Figure 1.2: Various examples of porous components produced through AM techniques: glass-ceramic scaffolds from DLP for biomedical applications (a),[34] ZSM-5 monoliths from robocasting for CO_2 separation (b)[9] and foamed-strut honeycombs for catalyst support produced through Direct Foam Writing (c).[25]

Chapter 2

Geopolymers and zeolites

Geopolymers are inorganic resins obtained from the dissolution of reactive aluminosilicate precursors in alkaline media. The term was coined by J. Davidovits in 1979 as an analogy to organic polymers, but prepared from traditional rock-forming or soil-based minerals. One of the best known precursors is metakaolin, which is obtained by calcination of kaolinite clay. High-temperature dehydroxylation leads to a reduction in Al coordination number and consequent buckling of the kaolinite layers resulting in a strained, amorphous structure which is highly reactive; other common precursors include coal fly ash and blast furnace slag. The activating solution is usually alkali- or alkali-silicate in nature, with sodium hydroxide or silicates being the most common although potassium-based solutions are also frequently used.[30]

A simplified mechanism for geopolymerisation is presented in Fig. 2.1.a. In the first stage the dissolution of precursors, which is only possible in the presence of electron donor ions such as alkaline metals, releases aluminate and silicate monomers of the type $\mathrm{Al(OH)}_4^-$ and $\mathrm{SiO}_x\mathrm{(OH)}_{4-x}^{x-}$ into the aqueous medium. These monomers react to form more and more complex structures until eventually saturation is reached and precipitation of an intermediate aluminosilicate gel product (Gel I) takes place. Initially the gel is rich in Al, as the Al-O bonds are weaker than Si-O and more easily severed, however as the extent of reaction proceeds the composition reequilibrates (Gel II) while connectivity increases. This model is however heavily simplified, as the aforementioned stages typically occur simultaneously: as a result, heterogeneous precipitation of various intermediates may occur on the surface of solid particles before complete dissolution. The final structure of a fully condensed geopolymer is that of an amorphous aluminosilicate network where alkaline cations such as Na^+ and K^+ balance the negative charges introduced by Al^{3+} substitution of Si^{4+}. Evaporation of water from the gel network results in the formation of voids which produce a tortuous mesoporous (2-50 nm) structure with strong adsorptive properties.[30]

One important property of geopolymers is that polycondensation can take place at temperatures as low as 0°C, although the reaction is greatly accelerated by heat. This characteristic allows to obtain dense bodies without the high temperatures traditionally associated with ceramics processing, and makes geopolymers attractive as a replacement for cement-based binders in the building industry due to their significant fire resistance and chemical durability and greatly reduced CO_2 emissions compared to cement manufacturing. Other applications include thermal insulation as foams, immobilisation of toxic waste[10] and passive cooling of environments by evaporation of water.[13] Sazama et al.[33] investigated the use of ion-exchanged geopolymers as heterogeneous catalysts and reported comparable performances to commercial V_2O_5/Al_2O_3 catalysts for NO_x conversion at a fraction of the manufacturing cost and complexity.

Zeolites are microporous aluminosilicates, characterised by highly ordered channel structures with molecular dimensions (0.3-2 nm), which are widely used in separation and catalysis due to their high surface area and selectivity.[19] To date 245 unique zeolite frameworks have been synthesised, of which about 40 are also naturally occurring, but over two-million structures are present in the Hypothetical Zeolite Databasecite[23] maintained by the International Zeolite Association (IZA) which also assigns the official three-letter framework codes to zeolites obtained from verified syntheses. Common zeolite frameworks are displayed in Fig. 2.1.b-e. Zeolite A (LTA framework) is composed of cage structures (called β-cages) arranged around a bigger α-cavity which is accessible to molecules larger than water via a three-dimensional channel system defined by 8-ring pores. In the context of zeolite frameworks the term ”n-ring” is used to describe channels which are constructed from n Si or Al atoms, while the bridging O atoms are usually just implied and not shown in depictions for simplicity. On the other hand the β-cages are inaccessible to molecules larger than water due to their 6-ring apertures. Zeolite X (for $1<\text{Si/Al}<1.5$) or Y (for $\text{Si/Al}>1.5$) belong to the FAU framework, termed after the natural analogue faujasite, and are some of the most studied frameworks thanks to the arrangement of the β-cages forming a large supercavity delimited by three-dimensional 12-ring pores: this feature gives FAU zeolites excellent adsorption and ion exchange capabilities, and additionally they can be made highly siliceous by post-synthesis dealumination steps yielding superior chemical and thermal stability and catalytic properties. Chabazite (CHA framework) is a natural zeolite, although several synthetic variants have been produced, which is characterised by the presence of a large cage accessible through 8-ring channels. It is most commonly found in basaltic rocks[6] and it is widely used in agriculture due to its low cost and moisture and nutrient retention capabilities.[40] Finally ZSM-5 (MFI framework) is a highly advanced synthetic zeolite which features straight 10-ring channels along the [0 1 0] direction and zig-zag channels in [1 0 0] and [0 0 1]. ZSM-5 is highly siliceous (Si/Al$>$10) and unlike most other zeolites it is markedly hydrophobic and organophilic.[19] It is used in the petrochemical industry for catalysis of hydrocarbon isomerisation and alkylation, which it accomplishes due to size-selectivity mechanisms.[12]

Zeolite synthesis is achieved through hydrothermal treatment of dilute aluminosilicate gels. Only a handful of structures (such as LTA, FAU, hydroxysodalite SOD and gismondine GIS) can be obtained without the use of seeding or appropriate structure-directing agents (SDAs), usually complex organic molecules which promote nucleation of a particular framework by negative templating of the micropore structure through steric hindrance; such additives must then be removed in a successive calcination step.[18]

Geopolymers and zeolites are closely linked, to the point that they are often considered to be the amorphous/crystalline equivalent of the other. Zeolite crystallisation during ageing of geopolymers is a well known phenomenon[30] and in fact it is believed that geopolymers are actually composed of various aggregates of nano-zeolites which are too small to produce crystalline X-ray diffraction.[29]

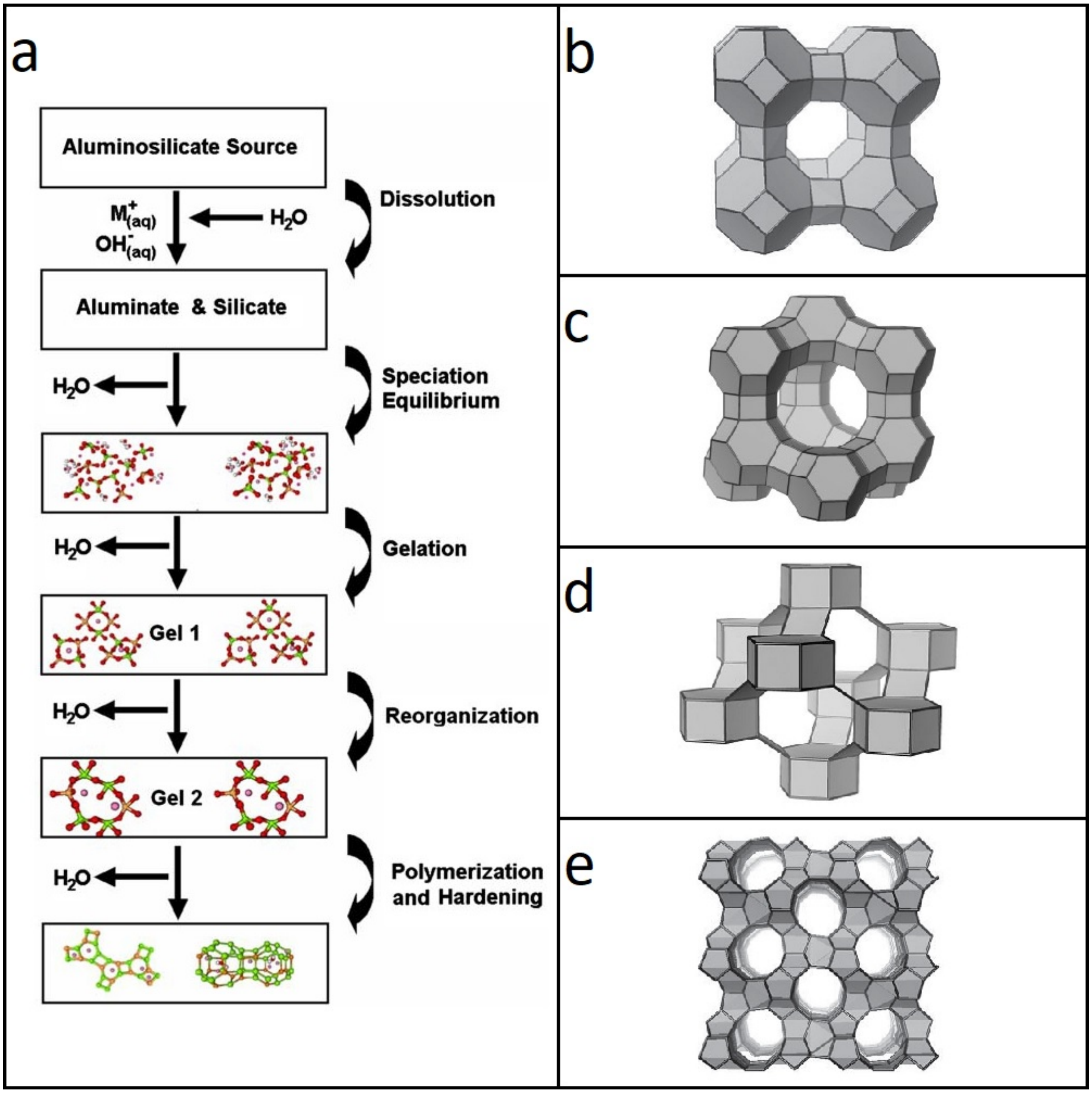

Figure 2.1: Proposed mechanism for geopolymerisation (a)[11] and structures of some of the most common zeolites, with edges indicating (Si,Al)-O-(Si,Al) bonds: LTA (b), FAU (c), CHA (d) and MFI (e).[19]

Chapter 3

Applications of porous materials

In their most immediate definition all porous materials may be though of as air-solid composites. The presence of air pockets in a solid allows for reduction of physical phenomena which require a continuity of material such as thermal conductivity. Thus foamed structures, especially polymeric in nature due to low costs, are widely used as thermal and acoustic insulators.[28] The IUPAC[22] further divides porosity into three main categories (micro-, meso- and macropores) mainly based on the interpretation of adsorption isotherms. Specifically:

- micropores (d $<$ 2 nm) exhibit monolayer or quasi-monolayer adsorption due to limited space
- mesopores (2 nm $<$ d $<$ 50 nm) are large enough that the gas may condense on the walls and occlude the pore
- macropores (d $>$ 50 nm) are large enough that filling due to condensed gas cannot occur at the temperatures and pressures used for gas adsorption isotherms

The use of zeolites is widespread in separation and catalysis due to their unique advantage of offering high specific surface area owing to a strongly microporous structure and significant selectivity at the molecular level thanks to the great variety of available framework morphologies and channel structures.[19] A development of zeolite technology was the introduction of Metal-Organic Frameworks (MOFs). MOFs (Fig. 3.1.b) are composed of metal ions or clusters which are linked together by bridging organic molecules, forming complex structures which often display the same frameworks geometry of some zeolites but allow for the presence of pores and channels in the very first mesopore region ($\approx$ 2-5 nm). Like zeolites, they are synthesised through hydrothermal or solvothermal treatment and display significant potential for applications in separation, catalysis and energy storage in fuel cells.[3]

Hierarchically porous materials display porosity on multiple scales. This allows for increased activity and synergic effects of the various systems, such that e.g. mesoporosity may minimise diffusion barriers and provide enhanced mass transport to a catalytically active microporous system. Moreover such materials are suitable to be produced through a variety of techniques (such as templating, phase separation, selective leaching and zeolitisation) allowing for great flexibility in morphology and final properties.[39]

Fukasawa et al.[17] introduced the use of freeze-drying for the synthesis of hierarchically porous ceramics, and the technique has since been investigated with great interest.[39] In freeze-drying a ceramic slurry is subjected to directional solidification such that the solvent is made to solidify with the appropriate geometry to provide a template of the desired pore structure. As solidification proceeds, the ceramic particles are rejected by the solvent and accumulate between the crystals forming the walls of the pore structure; the solvent is then sublimated and the part subjected to sintering to obtain a solid porous ceramic. By careful control of solidification kinetics it is possible to obtain hierarchical porosities such as the one shown in Fig. 3.1.b: it can be seen from the SEM micrographs that dendritic growth of ice crystals leads to a relatively coarse pore structure in the vertical direction, corresponding to the primary dendritic arms, while in the horizontal direction the secondary arms produce porosity on a smaller scale. The method is environmentally friendly, as water is frequently used as a solvent, and well suited for manufacturing highly porous catalyst supports.

Bouizi et al.[4] reported the synthesis of micro-microporous hierarchical systems consisting of core-shell zeolitic structures (Fig. 3.1.c. Zeolites with high selectivity, such as ZSM-5, tend to exhibit poor adsorption storage while frameworks like FAU which possess large cavities for storage have poor selectivity. To solve this problem, they introduced a system based on a high-storage core of zeolite β (BEA framework) over which a thin nanocrystalline ZSM-5 shell was grown. The shell provides separation of the desired species which are then stored in the core.

This thesis project aims to investigate the synthesis and properties of hierarchically porous geopolymer-zeolite composites with high water adsorption for applications in desiccation of natural gas streams. The use of robocasting allows introduction of tailored macroporosity which is accompanied by mesoporosity from the geopolymer matrix and microporosity from the zeolitic filler.

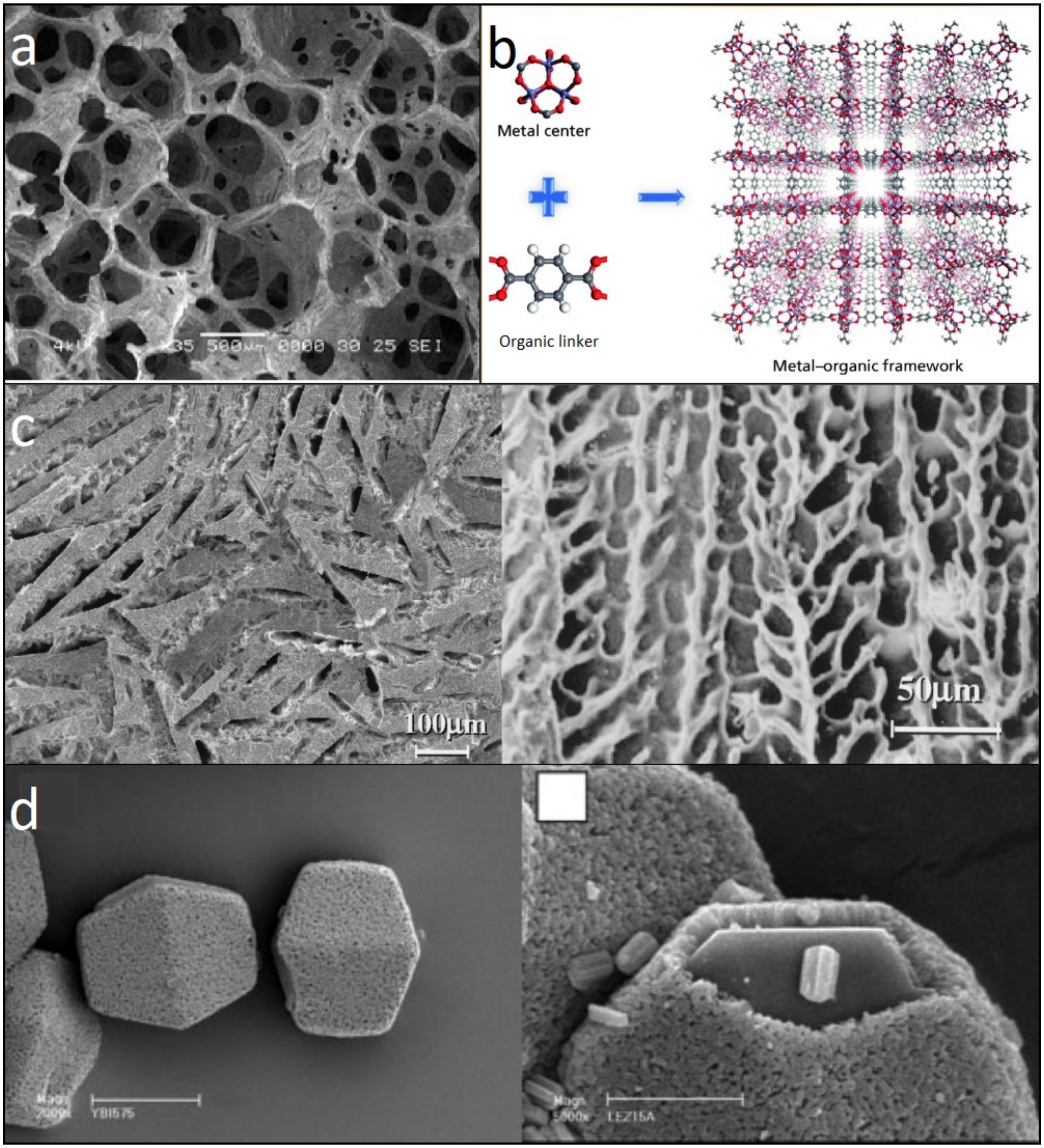

Figure 3.1: Various examples of porous solids: PU foam for thermal and acoustic insulation (b),[15] MOFs for catalysis and gas separation (b),[41] horizontal (left) and vertical (right) cross sections of a hierarchically porous ceramic by directional freeze casting for catalyst support applications (c)[17] and core-shell zeolite microcomposites for gas separation and storage (d).[4]

Chapter 4

Experimental procedure

4.1 3D model design

The design of appropriate CAD models for the DIW of ceramic slurries presents some notable differences compared to traditional polymer FDM. In the latter case, fully solid models are often fed to a slicing software (such as Slic3r) which automatically converts the CAD into a closed shell containing the requested infill pattern and density, then proceeds to slice it in horizontal layers and generate the G-code required by the printer. This method has the obvious advantage of being able to autonomously produce a variety of printer-ready designs, provided a good amount of control of the infill architecture, but the complex rheological behaviour of pre-ceramic slurries requires a more rigid approach. Abrupt movements of the printing head should be avoided, as the printed ink is only transiently solid and easily deforms if the filament is pulled. At the end of a layer, any transition movements should be carried out outside the perimeter of the lattice to ensure that the structure is left undisturbed: this is easily obtained by designing wide turns around the object whenever the end point of a layer and the origin of the subsequent one are far apart in the x-y plane. Provided a gap of a few millimetres is left between such support structure and the work, the excess material is easily removed after curing with no damage to the final print.

Two beam lattice geometries were produced to test for compression strength (S90 design) and gas permeability (C90 design). As shown in Fig. 4.1.b and 4.1.c, both were designed on Rhinoceros 5 as a single continuous line mimicking the path of the extrusion head during printing allowing to maintain complete control over its movement. The path was then polygonalised and converted to a series of consecutive G-code movements through a custom script implemented in Grasshopper/Silkworm. In both S90 and C90 each layer consisted of parallel lines spaced at 1.6 mm, aiming for a 50% geometrical porosity with a 0.8 mm filament, and is followed by an identical layer which is rotated in the x-y plane by 90° (Fig 4.1.a). The layer thickness was chosen as 0.6 mm to ensure good adhesion. In S90, this basic 0°/90° block was repeated through the height of the print to generate an orthogonal beam lattice with interconnected porosity and straight channels in the z-direction, and with dimension 20x20x7.2 mm (twelve layers). The second geometry (C90) was primarily designed to investigate the gas permeability performance of a 3D-printed porous monolith. In this case the specimens were designed to fit inside a pipe for pressure drop measurements, and have dimensions ⌀30x43.2 mm. Thirty-six 0°/90° blocks were progressively rotated by 5° to yield a more tortuous porosity with twisted channels as this would be needed to expose more gas to the surface of the monolith during service, although no attempt was made to further optimise the geometry using CFD simulations due to the preliminary nature of this study. Unlike S90, inter-layer transition is more complicated in C90 and the head needs to circle around almost half of the perimeter before being able to re-enter the upper layer at the correct position (Fig. 4.1.d). Models representing the final shape of S90 and C90 are displayed in Fig. 4.1.e and 4.1.f.

4.2 Metakaolin-based inks

Addition of commercial zeolites to a metakaolin-based pre-geopolymeric slurry constituted the first and most direct approach to the synthesis of a geopolymer-zeolite ink. Metakaolin has low cost and wide availability, and its role as a geopolymer precursor is very well documented.[10] The material used was Argical 1200S (provided by Bal-Co) with a mean particle size of 2 μm, SiO_2/Al_2O_3 molar ratio of 2.39 and a 6 wt.% fraction of other oxides, mainly Fe_2O_3 and TiO_2. The activating solution was formulated to correct the SiO_2/Al_2O_3 ratio and prepared by mixing sodium silicate (SS2942 by Ingessil), NaOH (Sigma Aldrich) and water while cooling to counter the effects of the exothermic dissolution of NaOH. The rheological properties of the viscous slurry obtained from the two-part geopolymer mixture were adjusted with the addition of an inorganic clay additive, sodium bentonite, in order to obtain a pseudoplastic paste described by a Herschel-Bulkley fluid model.

Three different zeolite powders were added to the geopolymer mixture, with the intent of probing their effects on the mechanical and functional properties of the monoliths and on their performance as adsorbents. A brief summary of their characteristics is given below, with detailed characterisation in Chapter 5:

- a synthetic NH_4-exchanged ZSM-5 zeolite (MFI framework) supplied by Clariant, primarily used in the petrochemical industry as heterogeneous catalyst
- a clay mixture containing 65 wt.% of natural chabazite (CHA framework) supplied by Zeolite-Italia used as water and nutrient adsorbent in agricolture
- a synthetic, nanocrystalline zeolite X (FAU framework) obtained through a geopolymer route, optimized for CO_2 adsorption[7]

The first ink (GP13) was formulated to investigate the feasibility of bentonite as a thickening additive, as in previous research projects in the Department polyethylene-glycol (PEG) was instead used in this capacity. Due to concerns over reduced specific surface area and lengthy removal treatments of the organic additive, it was necessary to determine whether an inorganic counterpart could be employed as effectively. The composition was chosen as $3.8SiO_2$-Na_2O-Al_2O_3-$13H_2O$ to conform to an analogous geopolymer previously printed with PEG. Subsequently three other inks were produced, each containing one of the zeolite powders mentioned above (GP-MFI, GP-CHA and GP-FAU). The most immediate effect of the addition of any solid filler to geopolymer slurries is a drastic increase in viscosity, enhanced in this case by the high surface area and water adsorption capabilities of zeolites, which in turn may require the formulation of more diluted inks. In order to limit this phenomenon the powders were stored in humid conditions (close to 100% R.U.), but the geopolymer composition had to be adjusted to $3.8SiO_2$-Na_2O-Al_2O_3-$18H_2O$ for the three zeolite-containing inks. Table 4.1 details the relative masses of precursors used to obtain geopolymers of both compositions. While in theory the amount of filler could be increased by varying the water content appropriately, inks with H_2O/Al_2O_3 ratios higher than 20 were found to separate readily during printing due to the high pressures involved, thus posing a limit to the zeolite fraction which could be immobilised in the matrix. The MFI zeolites in particular displayed the strongest water intake, with the mixture becoming almost powdery on addition of the metakaolin until dissolution started. The maximum amount of MFI filler which could be mixed with a $3.8SiO_2$-Na_2O-Al_2O_3-$18H_2O$ composition was found to be 20% of the geopolymer mass. It was thus decided to adopt the same filler ratio and matrix composition for the other zeolites as well, while varying the amount of bentonite required to obtain the correct rheological properties. An exception was made for the CHA filler, which was adjusted to keep the ratio of zeolite-geopolymer at 1/5 without considering the 35% impurity content. A summary of final compositions, normalised by the total wet mass, is displayed in Fig. 4.2.a.

Table 4.1: Relative masses of precursors to yield the compositions used in the MK-based inks, normalised for 100 g of total wet mass.

Composition	Notes	H2O (g)	SS2942 (g)	NaOH (g)	Argical 1200S (g)
3.8-1-13	GP13 only	6.2221	46.4846	6.5817	40.7116
3.8-1-18		17.7306	40.7942	5.7793	35.6960

A significant concern during the mixing process of the inks was the rapid onset of geopolymerisation once the metakaolin and activating solution were placed into contact. Polycondensation of the reactive aluminosilicate species is accompanied by a drastic increase in viscosity, with a noticeable effect on the rheology and required parameters for printing. In order to obtain consistent and reproducible ink properties, the addition of the metakaolin was carried out as the last step of the mixing process shortly before printing. As shown in Fig. 4.2.b, the activating solution was placed in agitation with an impeller mixer at low velocity (300 rpm), subsequently bentonite and the zeolite filler, if any, were added while velocity was increased slightly to 400 rpm. The mixture was then moved over an ice bath where the metakaolin was added, with mixer speed increased to 2200 rpm as the ink began to exhibit its final, heavily pseudoplastic behaviour. The low temperature and controlled duration (20 min) of this last stage of mixing helped ensure only negligible polycondensation occurred, thus limiting the effect of reaction time to the printing process. Following mixing the inks were stored in the fridge for 30 min to allow a more thorough dissolution of the metakaolin particles, then defoamed at 2000 rpm on a planetary mixer and moved to printing.

4.3 Aluminate-based inks

The synthesis of metakaolin-based inks is procedurally simple, but as discussed above there are limitations on the stability of water-rich compositions and thus on the allowable zeolite fraction. In order to circumvent this problem a second approach was pursued using a different geopolymer system based on sodium aluminate ($NaAlO_2$). Dilute aluminate gels are a common precursor in the synthesis of zeolites,[18] and a previous thesis project[24] indicated that systems with composition $2SiO_2$-Al_2O_3-Na_2O-$25H_2O$ obtained by combining a $NaAlO_2$ solution and a colloidal SiO_2 suspension could yield zeolitic (mainly zeolite A, LTA framework) or geopolymeric structures depending on curing conditions. A first attempt explored the possibility of printing inks of such composition directly, with bentonite, and then controlling the crystallisation of zeolites during curing to yield a final structure with a large fraction of active filler. In order to test the best curing conditions a batch was prepared and held for three days at room temperature, 40 °C and 75 °C, and in open or sealed containers. It was found that despite the initial low viscosity of the mixture a rheology suitable for printing was attained after a 12 h hold at 75 °C, although the fraction of bentonite (ca. 30 wt.%) was significantly higher than for the metakaolin-based inks. Several S90 models were successfully printed, however preliminary characterisation by XRD showed that the samples contained no amorphous fraction at all resulting in a poorly cohesive monolith. Moreover, it proved difficult to control crystallisation of this composition to yield a material which was only partly zeolitic. It is likely in this regard that the pre-printing treatment favoured the precipitation within the ink of zeolite seeds, which then promoted further crystallisation during curing.

In order to conserve some amorphous fraction after curing a second, non-stoichiometric gel with composition $3.8SiO_2$-Al_2O_3-Na_2O-$25H_2O$ was prepared. Unlike the zeolitic composition, this more concentrated geopolymeric mixture readily produced a gel with the required Herschel-Bulkley behaviour, although with insufficient viscosity and yield stress, and was found to crystallise a moderate fraction of zeolites when cured at 75°C in humid conditions. Printing was initially attempted through the addition of significant quantities of bentonite (ca. 30 wt.%), however given the intrinsically favourable rheology of the slurry it was soon apparent that other thickening additives could produce the required effect. The most appropriate choice appeared to be to use zeolites produced by the 2-1-25 composition as thickeners in the geopolymeric composition, thus increasing the final fraction of active filler and possibly promoting secondary crystallisation from the non-stoichiometric matrix.

As shown in Fig. 4.2.c, the synthesis of the aluminate-based ink is more complex as it involves the additional step of producing the filler. Although commercial zeolites could be used in the same way, in this case it was believed the significant affinity of the primary and secondary zeolites, in terms of compositions and curing conditions, would enhance the seeding effect. The aluminate solution for the zeolitic gel was prepared by mixing solid $NaAlO_2$ (SigmaAldrich) and water; cooling was again necessary as dissolution is exhothermic. After 30 min in refrigeration to complete solubilisation the solution was placed in agitation with an impeller mixer at 400 rpm, and the colloidal silica suspension (Ludox TM50 by Sigma Aldrich) was slowly dripped into it while progressively increasing mixing speed to 1200 rpm. Addition of the colloidal silica must be carried out very gradually as marked flocculation was observed on contact of the two precursors. After addition is complete the mixture was agitated at high speed (1500 rpm) for 10 min to remove any inhomogeneity, then cured at 75°C in sealed containers for three days.

The synthesis of the geopolymeric gel followed much the same procedure, although the more concentrated $NaAlO_2$ solution required up to 3 hours for solubilisation, and the higher viscosity of the final mixture an increased mixer speed (400-2000 rpm). The preiviously prepared zeolitic filler was then milled and sieved to 75 μm and added to the geopolymeric gel; 33 wt.% was determined to yield an acceptable rheology for printing. Due to the high water content of this ink no significant effect of polycondensation on the viscosity was observed during mixing and printing, thus mixing on ice and pre-printing refrigeration were deemed unnecessary. Defoaming was carried out using the same procedure as the MK-inks (2 min at 2000 rpm).

Table 4.2: Relative masses of precursors to yield the compositions used in the $NaAlO_2$-based inks, normalised for 100 g of total wet mass.

Composition	**Notes**	**H2O (g)**	**NaAlO2 (g)**	**Ludox TM50 (g)**
2-1-25	”zeolitic composition”	44.9596	22.3206	32.7198
3.8-1-25	”geopolymeric composition”	26.3551	19.4560	54.1890

4.4 Printing and curing

DIW was carried out with a Delta Turbo 2040 equipped with a LDM Extruder module for viscous clay slurries. The inks are placed in a syringe and pushed into the extruder by compressed air, which is adjusted manually, then forced through the 0.84 mm deposition nozzle by the rotation of the extruder screw. Operationally these two parameters, together with the movement speed of the nozzle, control deposition and need to be adjusted according to the properties of the ink to yield good-quality prints. Air pressure determines the flow of ink to the extruder, and has a direct effect on the thickness of the printed filament: if insufficient the filament is fragmented and has poor adhesion to the underlying layers, while if it is excessive design porosity is greatly reduced. Extruder flow and nozzle speed are determined while generating the G-code from the 3D model to give a constant volumetric flow through the nozzle, but they need to be adjusted as they do not take into account ink rheology. An ideal balance of flow and speed results in the filament being deposited in a state of light tension: this ensures that it remains well taut when passing over empty areas to keep porosity open. Once the correct balance has been determined they can both be carefully increased to reduce printing times, although some precision can be lost at high speed due to inaccurate positioning and rapid direction changes of the printing head. If the flow is insufficient to support the selected speed, the filament is placed in significant tension resulting in progressive shrinkage of each successive layer: this was particularly evident with the S90 designs, where the 90°turns at the end of each layer visibly constrained the parallelepipedal shape into a truncated pyramid. On the other hand excessive flow causes compression and buckling of the filament resulting in a print with poor tolerances and decreased porosity. Values of the printing parameters for the five inks, shown in Tab. 4.3, highlight the substantial variations in rheological properties between the various systems. The unfilled GP13 (due to lower water content) and GP-MFI in particular displayed high viscosities compared to the others: in their case defoaming could not be carried out as even in the short times considered heat from the motor would promote significant polycondensation with the associated increase in viscosity: these inks contained more air bubbles than the others, resulting in slightly more fragmented filaments. In the case of GP-MFI especially a cooling jacket was also employed around the syringe during printing. Several samples of the S90 design were produced for each ink to serve as compression test specimens, while the C90 design was only printed using the GP-CHA ink, as it only served to characterise the structure, due to its lower viscosity and generally easier management.

Table 4.3: Approximate printing parameters for the five inks: speed and flow are defined relative to the values expressed in the G-code (100); the table also shows whether defoaming and pre-printing refrigeration were carried out.

Ink	Speed	Flow	Air pressure (atm)	Defoaming (Y/N)	Refrigeration (Y/N)
GP13	100	180	1.5-2.5	N	Y
GP-MFI	100	200	2.5-3.5	N	Y
GP-CHA	100	150	0.8-1.3	Y	Y
GP-FAU	100	150	1.1-1.5	Y	Y
GP-LTA	100	150	0.7-1.2	Y	N

Following DIW the prints were cured at constant temperature and humidity. The effective conditions varied between inks due to different applications and requirements of the precursor system. The zeolite-filled MK-inks were cured for 20 days at room temperature (24-26°C) in a container maintained at 75% R.U.: this procedure aimed to exploit the low-temperature-setting capabilities of geopolymers thus avoiding costly heat treatments. GP13 was instead cured at 75°C in a sealed box for 2 days: this method was the same used for the previous 3.8-1-13 composition printed with PEG and thus necessary for comparison. On the other hand the curing parameters for GP-LTA were selected to maximise the secondary crystallisation of zeolites from the matrix, which required hot and humid conditions: coupled with negligible hardening at room-temperature, this factor determined the selected curing procedure at 75°C for 3 days in sealed containers. Images of the final monoliths are displayed in Fig. 4.3.

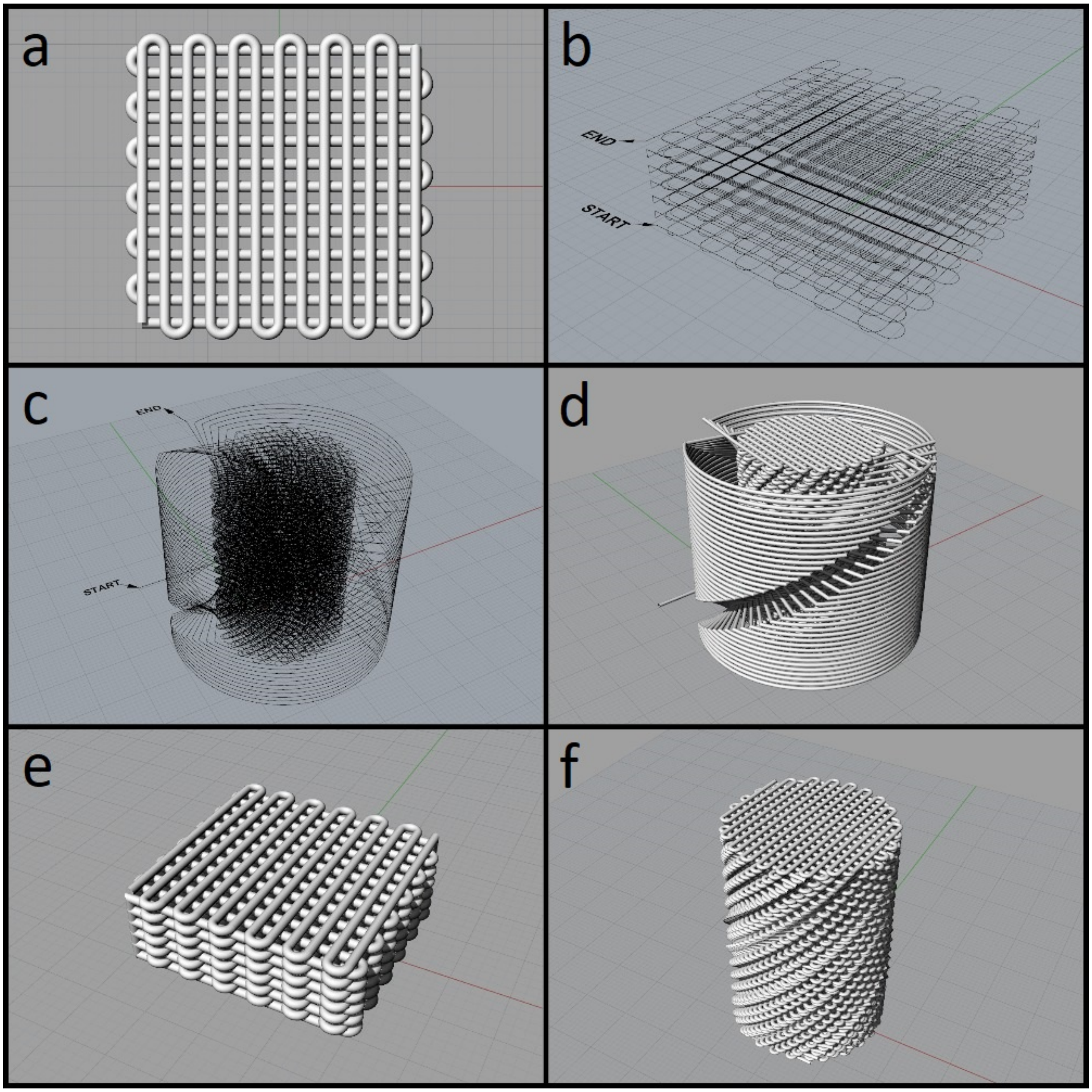

Figure 4.1: Various stages of the design process for the S90 and C90 models: detail of the 0°/90° block in the S90 design (a), printing head pathways for S90 (b) and C90 (c), C90 and support structure after printing (d), final designs after removal of eventual excess material (e, f). FIlament diameter is 0.8 mm.

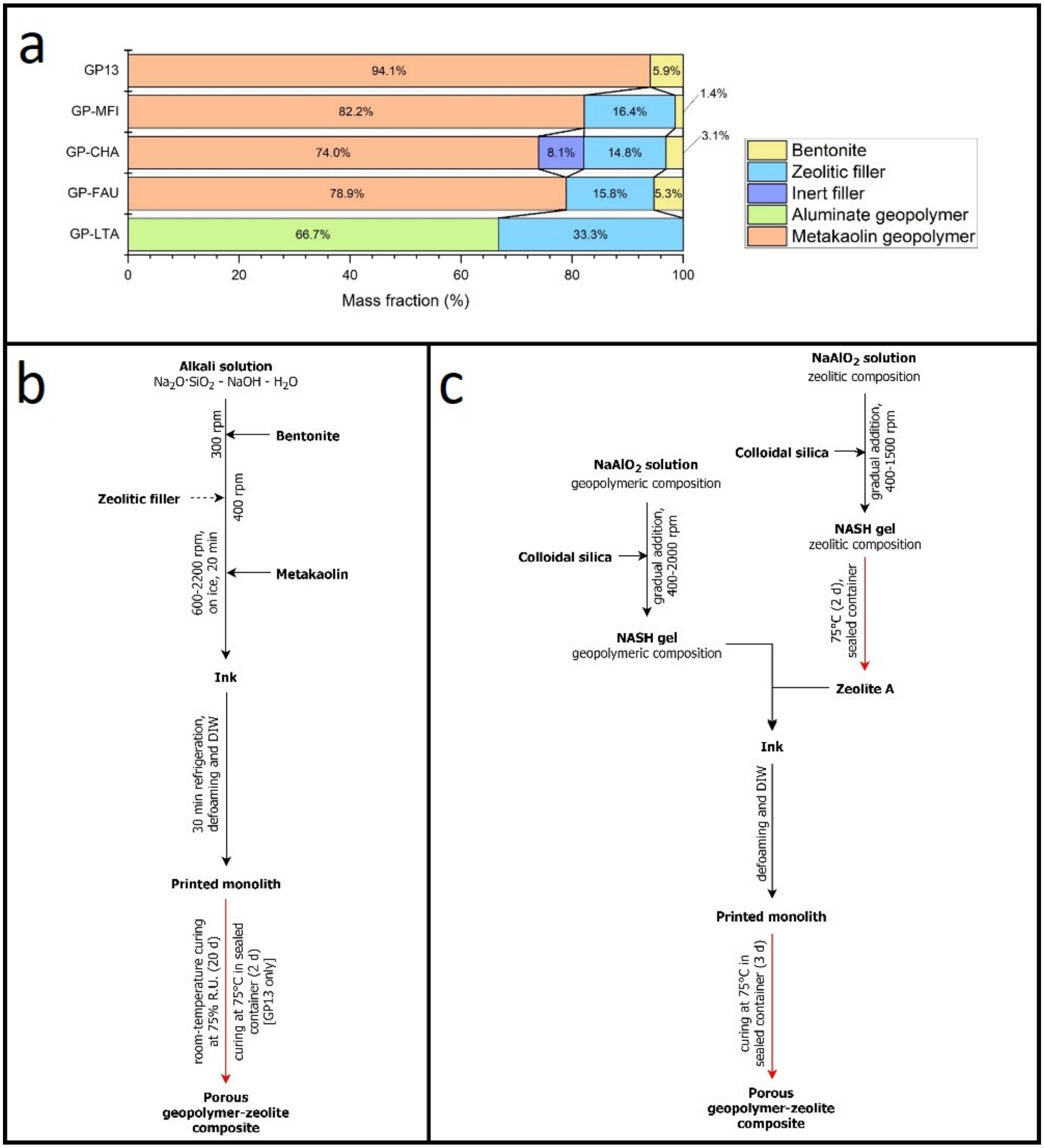

Figure 4.2: Summary of the experimental procedures: composition of the inks by mass on mixing (a), flow diagram for the production of porous geopolymer-zeolite monoliths with metakaolin- (b) and aluminate-based inks (c); red arrows indicate long (t > 24 h) steps in the production process.

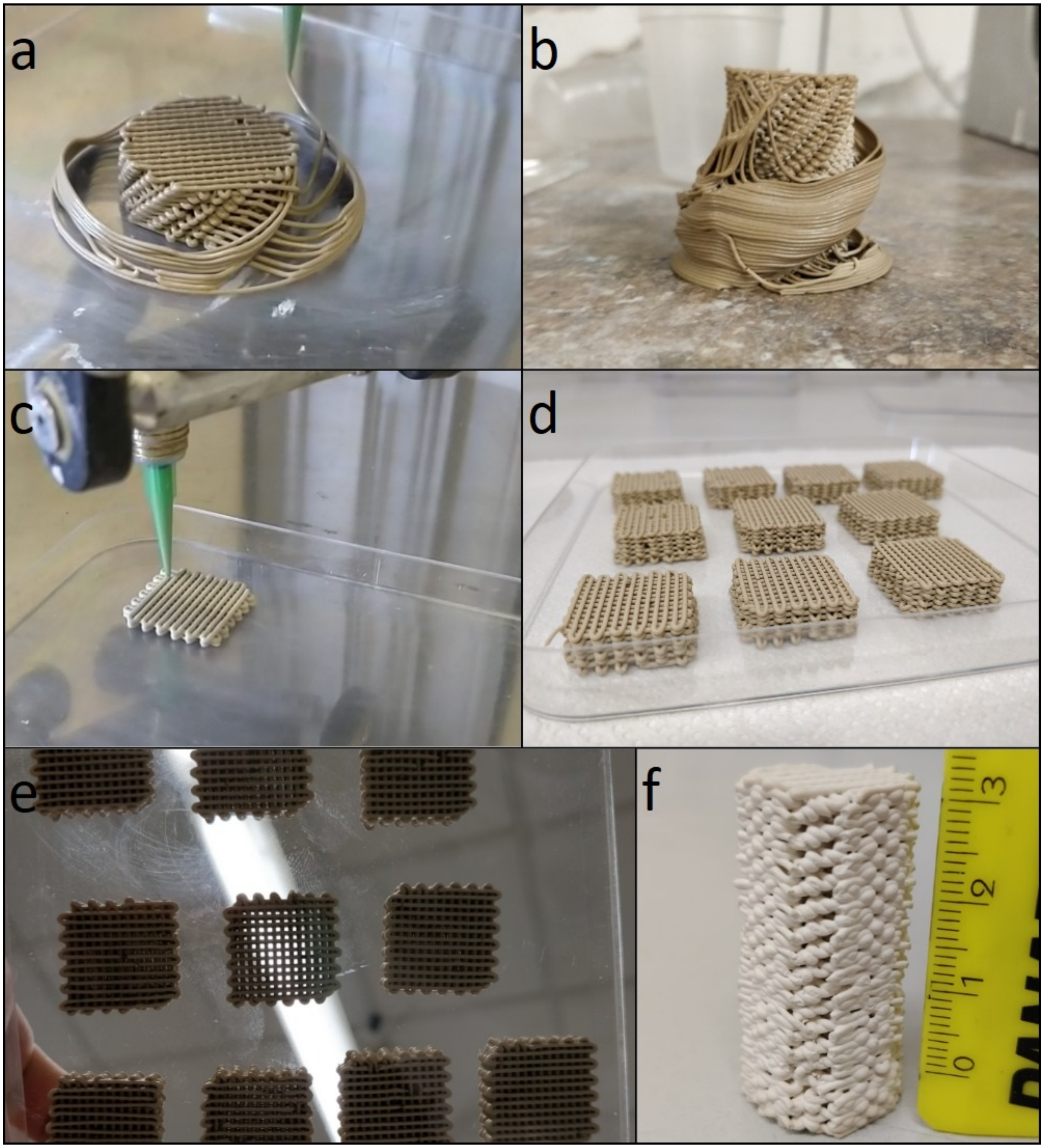

Figure 4.3: Selected images of the printing process and monoliths: C90 during printing (a) and after with support structure still attached (b), S90 during (c) and after printing (d) showing well open vertical channels (e) and a ⌀20x30 mm geometry printed with GP-MFI (f).

Chapter 5

Characterisation of the zeolitic fillers

5.1 Diffractometry

The identification of zeolitic phases through diffractometry is complicated by their intricate crystal structures as well as a general scarcity of available reference patterns on the Crystallography Open Database (COD). In these cases Match! was employed to obtain a preliminary identification of the phases involved, which was then refined by comparison to calculated diffraction patterns maintained by the International Zeolite Association (IZA).[38] In most cases a perfect match could not be obtained as framework codes are not strictly associated with a single specific material but rather to families of zeolites bearing the same crystal structure, and slight variations from the reference patterns in terms of peak positions and intensity could be observed. Despite this, framework codes were confirmed (for MFI, CHA and LTA) or identified (for FAU) with a high degree of certainty, even though in some cases further determination of the correct material required additional information.

The diffraction pattern for the MFI filler, displayed in Fig. 5.1.a, reveals a highly crystalline structure whose main reflections are entirely consistent with the reference pattern for ZSM-5 zeolite,[38] as expected by the high purity required for its catalytic applications. Although some of the minor peaks could not be unambiguously identified, the high intensity of the ZSM-5 diffraction lines indicates that impurity content, if any, is low and the discrepancies are likely explained through slight differences with the reference material.

On the other hand the CHA filler is only composed of 65 wt.% chabazite, with other impurities including volcanic glass (20 wt.%), pyroxene (4 wt.%), K-feldspar (4 wt.%) and phillipsite zeolite (2 wt.%).[40] Despite this, no such impurities could be successfully identified in the diffraction pattern (Fig. 5.1.b) and no amorphous halo was observed. The main reflections of pyroxene, K-feldspar and PHI zeolite all lie at around 28° and are probably collectively responsible for the unidentified peak complex in that region. It is important to note that the chabazite peaks, although all present, are consistently shifted by about +0.2° with regards to the reference pattern: given the natural origin of the filler, a possible explanation might be that the reference mineral was extracted in Iran,[6] while the one considered in this study is from Italy. Chabazite is known to display a large degree of flexibility in its structure,[1] which might lead to differences in the diffraction behaviour. Peak shifting could also be caused by incorrect sample preparation, however while small variations in the order of a few scan steps ($\pm$0.04 °) were indeed observed in repeated measurements of some of the samples, the significant magnitude in this case would appear to make the first explanation more likely.

Unlike the others, the FAU filler (Fig. 5.2.a) was supplied without indications on the nature of the framework and identification of the zeolite was necessary. A preliminary candidate selection was carried out through the use of an identification table[38] based on the main reflections of all currently synthesised zeolites, and subsequently refined through comparison with the calculated patterns. The highest peaks were found to belong to zeolite Na-X, of the FAU framework, although some of the others could not be identified. Unlike the other zeolites, the general peak intensity was found to be much lower in this case: the presence of a higher background as well as what seems to be an amorphous halo indicate that the geopolymeric route used in the synthesis of the powder only resulted in partial crystallisation of zeolite Na-X. Moreover some of the peaks appear broadened, confirming the nanocrystalline nature of the sample.

Identification of the zeolitic phases in the self-synthesised filler was necessary to validate the aluminate route. Zeolite A (LTA framework) is a common product of template-free aluminosilicate gels with Si/Al$\approx$1, and it had previously been shown to crystallise from the $2SiO_2$-Al_2O_3-Na_2O-$25H_2O$ system.[24] Indeed, the diffraction pattern (Fig. 5.2.b) exhibits high crystallinity and the main reflections were associated with the hydrated zeolite A reference pattern. A single, unmatched peak at 28° however indicated that another phase was present in lower amount. Zeolite crystallisation occurs through the formation of several unstable intermediates, and the complex and locally-changing chemistry of the environment often leads to competing precipitation of different structures in the absence of the appropriate SDAs. Maldonado et al.[21] showed that growth solutions with similar precursors cured at 100°C yielded zeolite P1 (GIS framework), X (FAU) or A (LTA) depending on composition. The Na-P1 reflections, as shown in Fig. 5.2, are consistent with the experimental pattern and explain the presence of the peak at 28°, corresponding to the main GIS line: although no phase quantification was attempted, the relative intensity to the LTA reflection at 30° suggests that it only constitutes a small fraction of the biphasic mixture.

5.2 Morphology and granulometry

The addition of zeolites to the geopolymer inks produced varied and at times counterintuitive effects on the slurries' rheology. In particular, given constant matrix composition, MFI zeolites produced an extremely viscous ink compared to FAU and CHA, even considering the higher total filler content of the latter. It is evident that in an attempt to explain these differences the role of particle granulometry and morphology cannot be neglected.

Given that all the zeolites appeared to be very fine, sieve analysis could not be attempted and examination through SEM seemed the most direct approach for determining particle size. The powders were observed in a FEI Quanta 200 in low vacuum (0.53 Torr) at 20.00 kV, with 300x and 2000x magnification (Fig. 5.3). A preliminary drying step for 12 h at 75°C was necessary to avoid excessive water evaporation in the vacuum of the sample chamber.

A quick comparison of the micrographs reveals granulometry to be somewhat similar between the zeolite powders, but with significantly different morphology and size distribution. The MFI filler is composed of nodular particles with diameter in the 1-10 μm range and relatively narrow distribution: it is possible the tight packing of the powder, which was noticed during handling and confirmed from the micrographs, resulted in the strong thickening effect observed in the GP-MFI ink. On the other hand the CHA filler contains similarly sized, pseudocubic chabazite crystals (two examples are highlighted in Fig. 5.3.b) which may be dispersed or aggregated. A number of larger particles, up to 70 μm in diameter, were observed as well as lamellar, spherical and irregular shapes which could not be unambiguously attributed to the various impurities listed in the data sheet.

The FAU and LTA fillers display some similarities likely deriving from their synthesis route using dense geopolymeric gels: both cases present coarser particles in the 5-75 μm range, probably amorphous in nature, which appear to be covered in sub-micron surface features identified as the zeolitic fraction. In LTA some of the crystals clearly displayed the cubic habit of zeolite A at higher magnifications, while in FAU they remained barely visible but compatible with the nanocrystalline-amorphous model emerged from the diffraction pattern. The different nature of the geopolymer growth gel is evident in the overall morphology of the two powders: the metakaolin precursor used for the synthesis of the FAU filler[7] produced nodular and seemingly dense primary particles. On the other hand, the aluminate gel yielded open and highly porous structures which appear to have formed by agglomeration and interpenetration of the zeolitic crystals during growth. A few spheroidal particles about 8 μm in diameter are also visible in the LTA filler at low magnification: hydroxy-sodalite (SOD framework) is known to crystallise with ”thread-ball” morphology and its synthesis is somewhat compatible with the conditions considered,[16] but no match was found with the reference XRD pattern.

5.3 Water adsorption

Table 5.1: TGA-derived water adsorption capabilities of GP13 and the zeolitic fillers, expressed as a percentage of the dry mass; T_x denotes the temperature at which divergence from the initial linear regime is observed.

Material	**T_x (°C)**	**H_2O_{ads} (%)**
GP13	74	7
MFI filler	57	11
CHA filler	70	16
FAU filler	63	30
LTA filler	69	21

High water adsorption is a primary characteristic of zeolites due to their porous structure and high surface area. In fact, characterisation of this property held utmost importance given the proposed application of the monoliths as natural gas desiccants, and several attempts were made to estimate it both by determining mass changes after permanence in humid environments and with equipment designed to measure the loss-on-drying of polymeric granulates. In each case the results had poor consistency and reliability, so it instead appeared more sensible to simply obtain a qualitative performance comparison by thermogravimetric analysis of the wet powders.

A sample of each zeolite, as well as powdered GP13 for reference, was dried for 12 h at 150°C, then mixed with water in an amount equal to 50% of the dried powder weight. TGA was carried out in air between room temperature and 700°C with a 2°C/min ramp; before analysis the samples were kept in sealed containers for 24 h to ensure thorough hydration.

All plots exhibit rapid mass decrease in the initial stages of heating, corresponding to evaporation of interstitial free water which was added to the powders in excess. A second regime, following a marked slope change around 60-70°C, is compatible with the loss of coordinated water adsorbed within the micropores, which occurs at higher temperatures. A clear distinction between the two steps could not be obtained, and the matter is further complicated by the presence of multiple distinct physisorption sites in zeolitic structures which preferentially dehydrate at different temperatures[19] together with the complex interactions between water molecules and adsorbed cations. The DSC plots show the sharp endothermic peak in the range of 20-100°C caused by the large amount of excess capillary water, but the poor signal/noise ratio precludes accurate analysis of the high-temperature behaviour. MFI (Fig. 5.4.a) exhibits two endothermic peaks at 220°C and 310°C accompanied by slight mass reductions, the latter of which might correspond to chemidesorption; a similar phenomenon was observed for CHA at 350°C (Fig. 5.4.b), but not for FAU, LTA or GP13 (Fig. 5.5.a and .b and Fig. 5.6.a respectively). Given the qualitative nature of this particular analysis, the abrupt slope change at $\approx$60°C appeared to be the most distinctive feature by which a comparison of the five samples could be attempted: it was in this case postulated that the first steep trait of the curve was associated with the excess free water while the second to mechanisms related to micropore adsorption, which are of more interest for the purposes of this study. The two quasilinear branches around the turning point were extrapolated and the intersection taken as the delimiter between the two regimes. The projected mass at the intersection, once divided by the dry mass measured at 700°C, was considered an estimate of the samples' adsorption capabilities by which a performance assessment could be reasonably made. Tab 5.1 shows mass and temperature coordinates for the intersection points of the five samples. As expected, GP13 performs worse than the zeolitic fillers but still retains a moderate amount (7%) of adsorbed water: this is an effect of the strongly hydrophilic and mesoporous nature of geopolymers which leads to significant moisture affinity.[10] The ability to simultaneously provide mechanical support for the zeolitic fillers and offer additional water adsorption further validates the choice of a geopolymeric matrix.

A comparison of TGA curves expressed as fraction of the dry mass for all samples is presented in Fig. 5.6.b. FAU and LTA exhibited the most significant adsorption (30% and 21% respectively), of which the apparently higher surface area observed by SEM may be a contributor. CHA performed relatively well (16%) considering its lower purity and natural origin, although this was expected since commercial application of the filler is moisture retention. Conversely MFI zeolites are employed as catalysts in hydrocarbon isomerisation and transalkylation reactions and for general separation and catalysis in humid environments: this is possible due to the highly organophilic and hydrophobic character of such zeolites,[19] which is fully evident in the low adsorption (11%) measured by TGA. The scarce water affinity and relatively coarse granulometry observed through SEM confirm that the thickening effect in GP-MFI ink is simply caused by close packing of the powder. In all cases the curves show that significant desorption only occurred in the initial stage of heating: discounting interstitial water, mass decreases rapidly up to 200°C before settling in a weakly descending trend up to the end of the selected TGA range (700°C): this suggests that regeneration could be performed at temperatures of 250°C or even as low as 200°C while still removing the vast majority of adsorbed water, thus allowing to avoid the significant costs of treatments at higher temperatures.

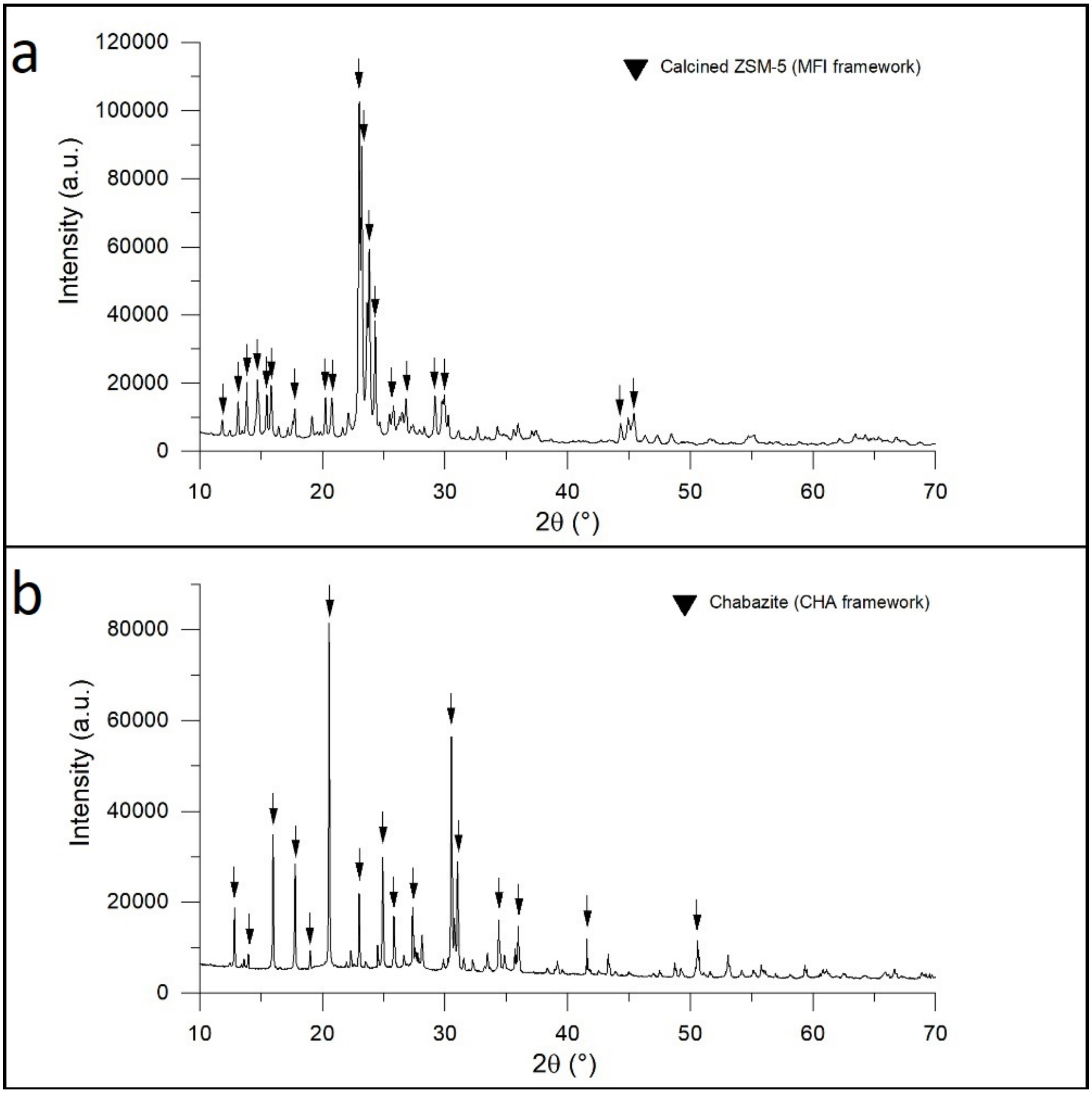

Figure 5.1: Diffraction patterns for the MFI (a) and CHA fillers (b); collected with CuKα radiation, 0.02° step size and 0.6°/min scan speed.

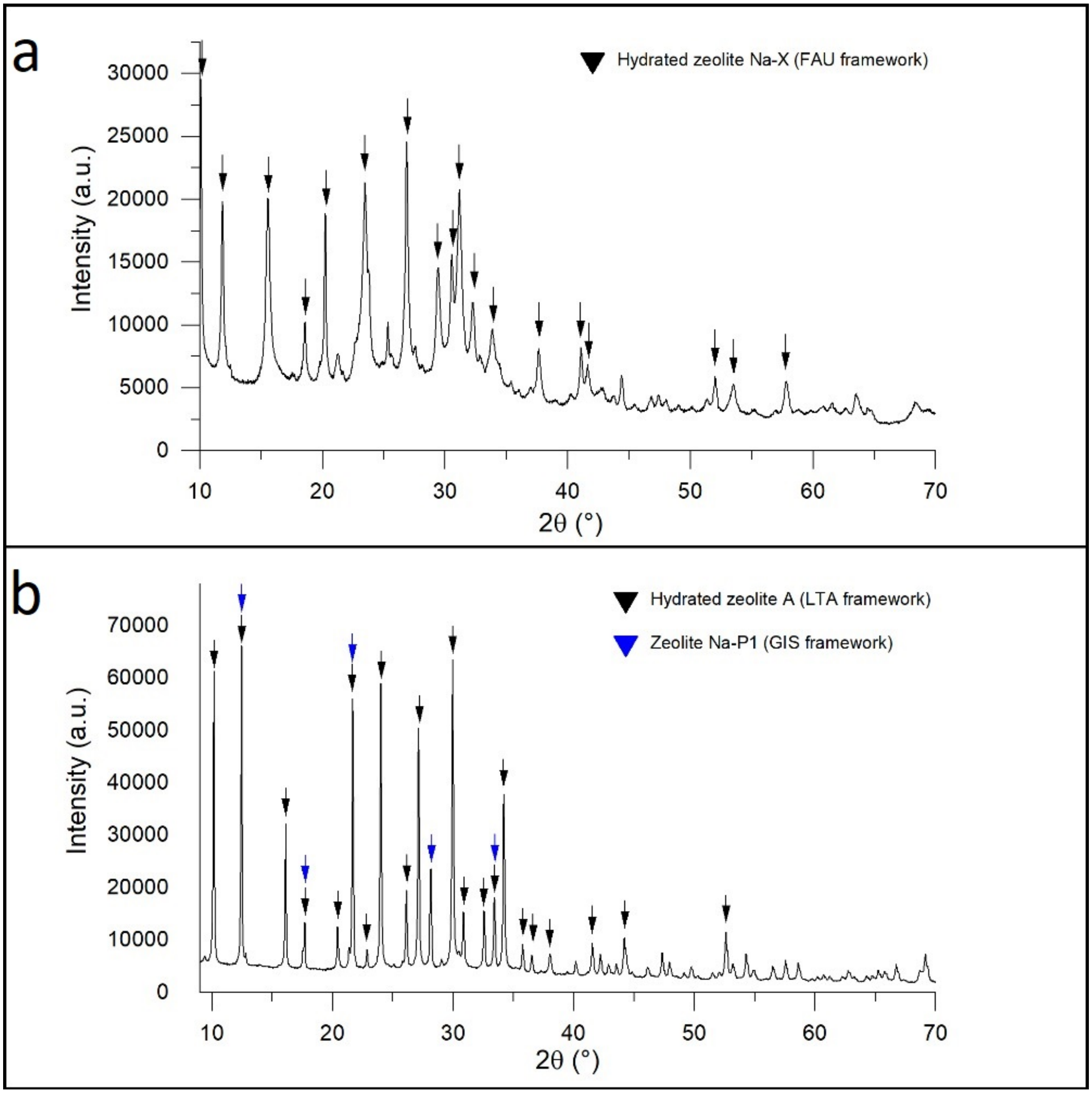

Figure 5.2: Diffraction patterns for the FAU (a) and LTA fillers (b); collected with CuKα radiation, 0.02° step size and 0.6°/min scan speed.

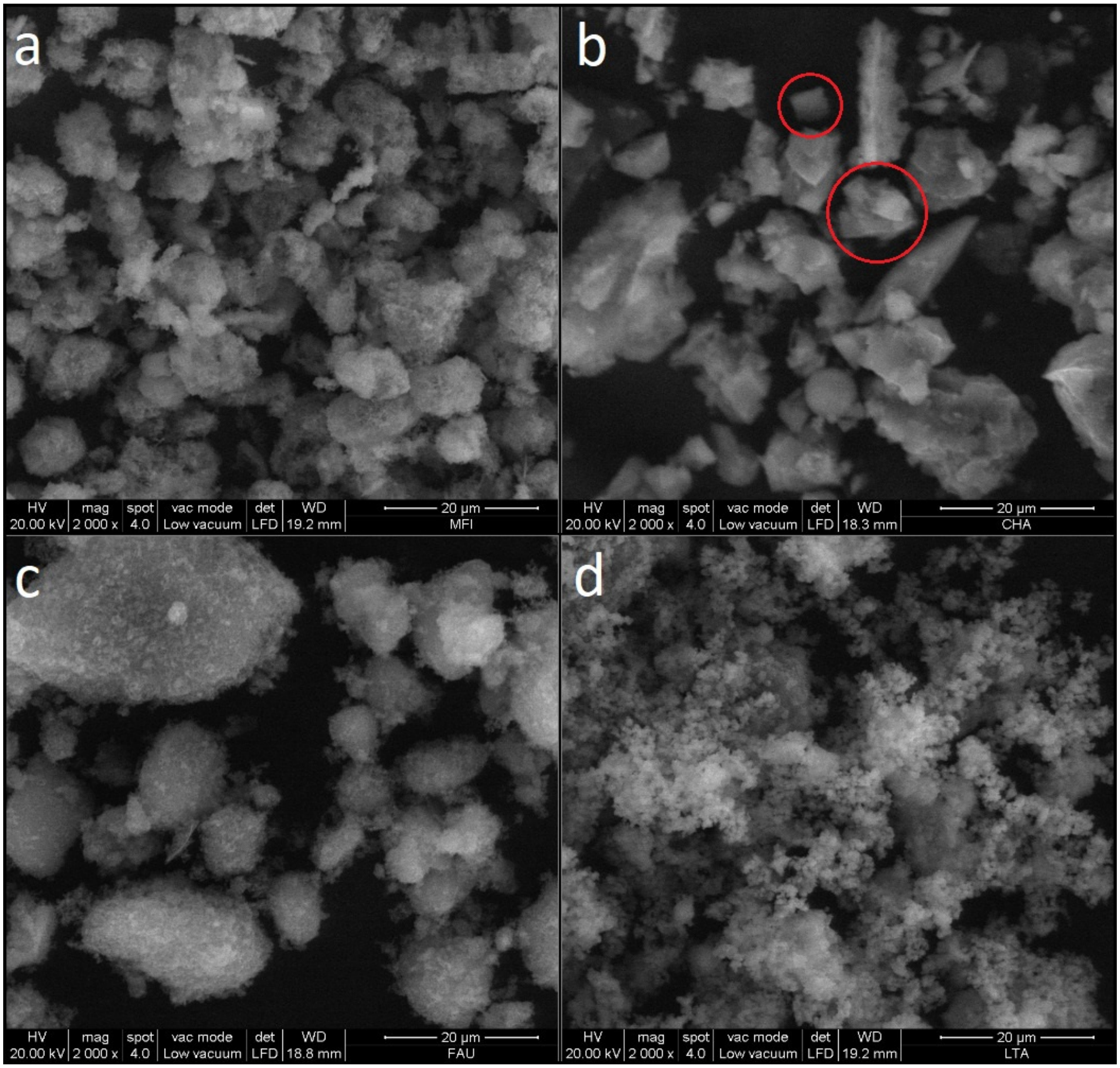

Figure 5.3: SE-SEM micrographs of the zeolite powders used as fillers: MFI (a), CHA (b) with pseudocubic chabazite crystals highlighted in red, FAU (c) and LTA (d); 2000x magnification

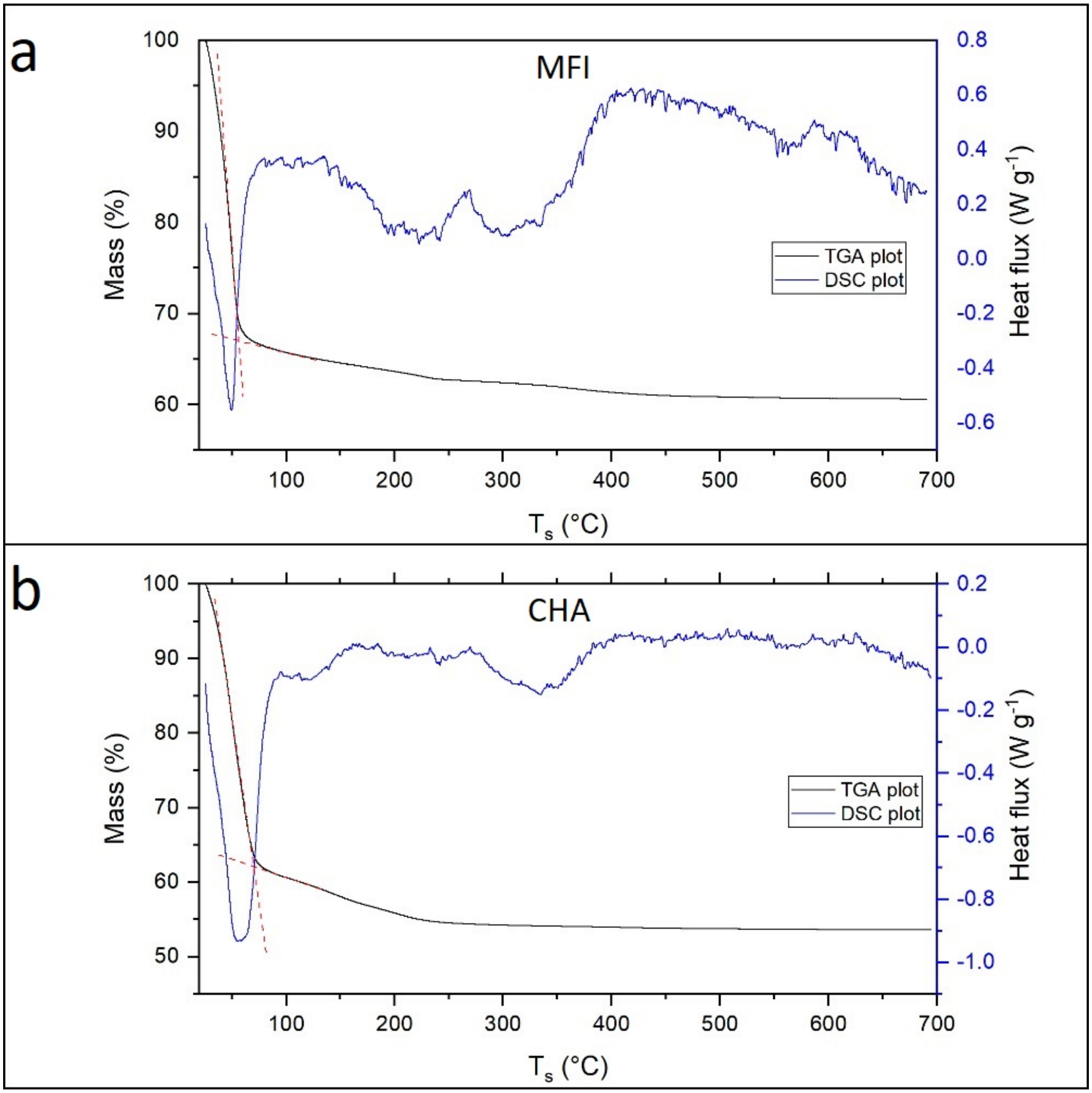

Figure 5.4: TGA-DSC plots for MFI (a) and CHA (b) fillers, taken in air at 2°C/min.

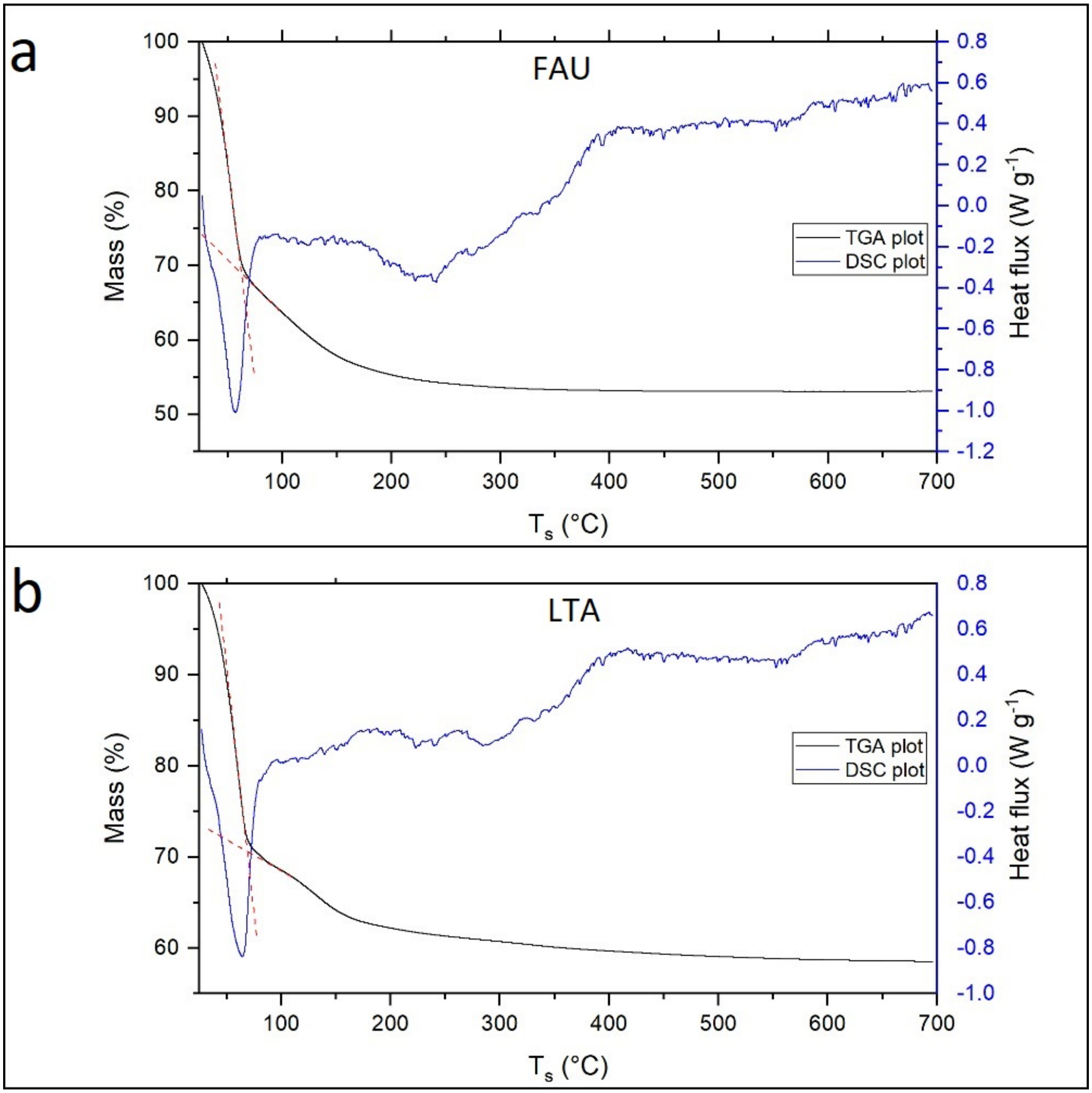

Figure 5.5: TGA-DSC plots for FAU (a) and LTA (b) fillers, taken in air at 2°C/min.

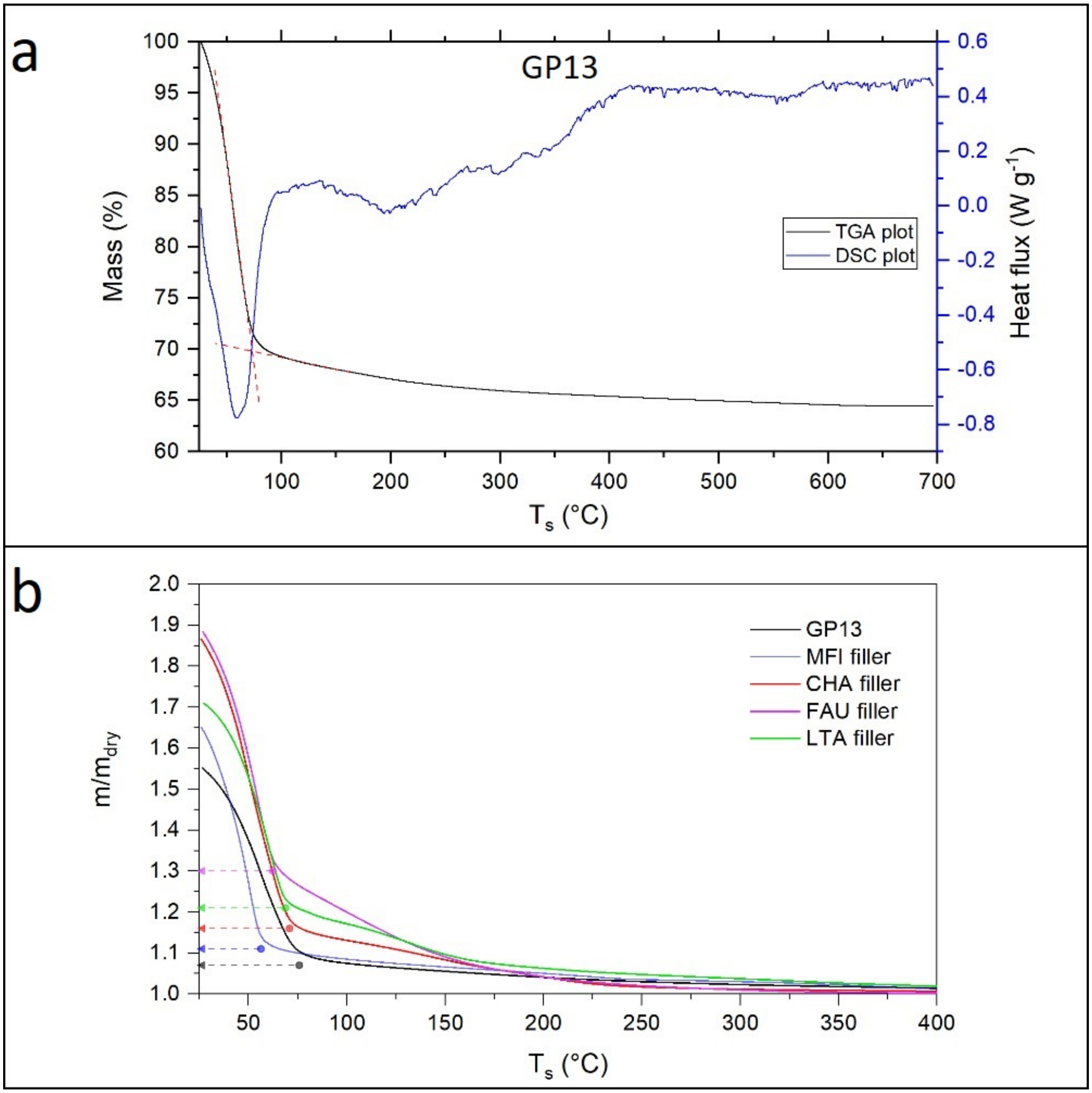

Figure 5.6: TGA-DSC plot for GP13 (a) taken in air at 2°C/min and comparison of the samples' behaviour through TGA curves normalised by the dry mass at 700°C (b); arrows indicate the point at which coordinated water desorption was estimated to begin.

Chapter 6

Microscopy

Optimisation of ink rheology is not a trivial task. Even small amounts of bentonite were found to have a marked effect on the slurries' viscosity which is of paramount importance in obtaining high-quality prints with good geometrical tolerances. Generally speaking there is a range of allowable additive content whose lower limit is obviously determined by visible collapse of the structures during printing. As bentonite content is increased, so do the mechanical properties of the ink which permit to achieve more regular filament position and spacing and well-open porosity, as well as the possibility of designing taller structures without collapse. This is however accompanied by an increase of the air pressure and flow parameters which are required for DIW and by a reduction of the available printing window due to the rapid evolution of viscosity during polycondensation, until eventually these values exceed what is allowed by the printer or special consideration must be taken to retard geopolymerisation e.g. through the use of a cooling system. GP13 and GP-MFI were on opposite ends of such viscosity interval, and while both retained acceptable tolerances and shape the differences between the two structures are evident. Fig. 6.1 displays a comparison of GP13 and GP-MFI structures through stereoimicrographs of some of their most important features. It can easily be seen that in GP13 filament diameter is larger and porosity is less open with respect to GP-MFI owing to the vastly different properties of the two inks. Comparison of one of the lateral pores near the base indicate that collapse of the structure under its own weight resulted in an approximate opening area of 0.1 mm^2, with a substantial reduction ($\approx 60\%$) compared to the 0.25 mm^2 of GP-MFI and a severe rounding effect. The latter, on the other hand, only displays limited reduction of porosity towards the base and an obviously more regular structure. Some smoothing of the nominally rectangular pore openings occurs anyway, however this is thought to be beneficial as it removes sharp notches which might act as crack initiation sites. It must be concluded from this brief analysis that the bentonite content in GP13 should have been increased slightly, based on microscopy, although some contribution to its reduced viscosity is also given by the absence of a filler.

Fracture surfaces of the filaments for all materials were also observed through SEM to characterise their apparent roughness and porosity. As with the fillers, a preliminary drying step at 75°C was found to be necessary to avoid degassing. One lattice of each type was cut in half, and one of the parts subjected to heat-treatment at 400°C for 2 h with 5°C/min ramp to simulate regeneration and evaluate the formation of cracks by comparison with the other. Although all samples exhibited some damage from the cutting process, only GP-FAU was found to have visibly suffered from the treatment: it is possible this is due to the higher water adsorption of the FAU filler and the consequent violent evaporation at high temperatures. This may be avoided however, as TGA showed lower-temperature regeneration treatments at 250°C should be effective in removing virtually all moisture. Fracture surface micrographs at various magnifications are presented for GP13 (Fig. 6.2), GP-MFI (Fig. 6.3), GP-CHA (Fig. 6.4), GP-FAU (Fig. 6.5) and GP-LTA (Fig. 6.6). At the lowest magnification all filaments present some closed porosity due to air bubbles trapped in the viscous inks, as best shown in Fig. 6.2.a. As discussed in Chapter 4 defoaming could not always be performed before printing due to the rapid onset of polycondensation in the heat generated by the mixer motor, thus the presence of some such closed porosity is unavoidable without the use of specialised equipment. As expected, at higher magnification all MK-based matrices appear visually similar, with rough and irregular surfaces and some macroporosity of approximately 5 μm diameter. Lamellar structures, visible especially in Fig. 6.2.c and Fig. 6.5.c, were attributed to bentonite while identification of the fillers was attempted but with scarce results due to the rough surfaces and low compositional contrast in BSE mode. A large filler particle is displayed in Fig. 6.5.b, although obviously belonging to the coarser and most likely amorphous fraction of the FAU powder as discussed in Section 5.2; in BSE mode it appears to conform to the matrix almost exactly, as expected from its similar chemical nature as a MK-based geopolymer. GP-LTA on the other hand displays a strikingly different surface morphology, close to the one observed for its filler: the structure seems to be composed of interpenetrating spheroidal particles with size below 1 μm and markedly increased macroporosity compared to the MK-geopolymers. Although the crystal habit could not be resolved, it is likely at least some of these spheroids are in fact primary or secondary LTA particles as evidenced by the striking resemblance with the filler micrograph presented earlier in Fig. 5.3.d.

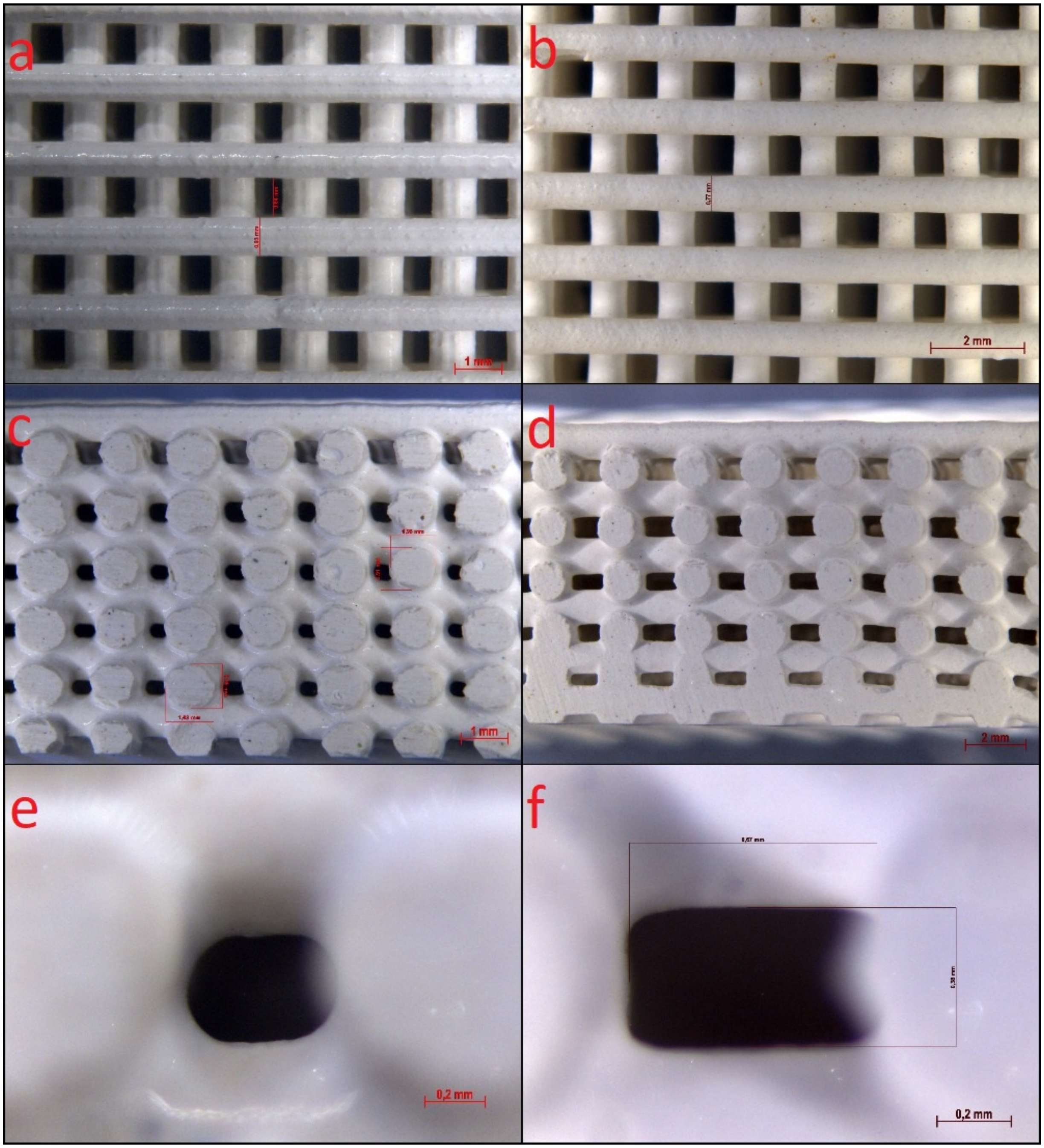

Figure 6.1: Stereoscopic micrographs showing the lattice structure printed with GP13 and GP-MFI: top face for GP13 (a) and GP-MFI (b), side face for GP13 (c) and GP-MFI (d), detail of lateral pore opening for GP13 (e) and GP-MFI (f).

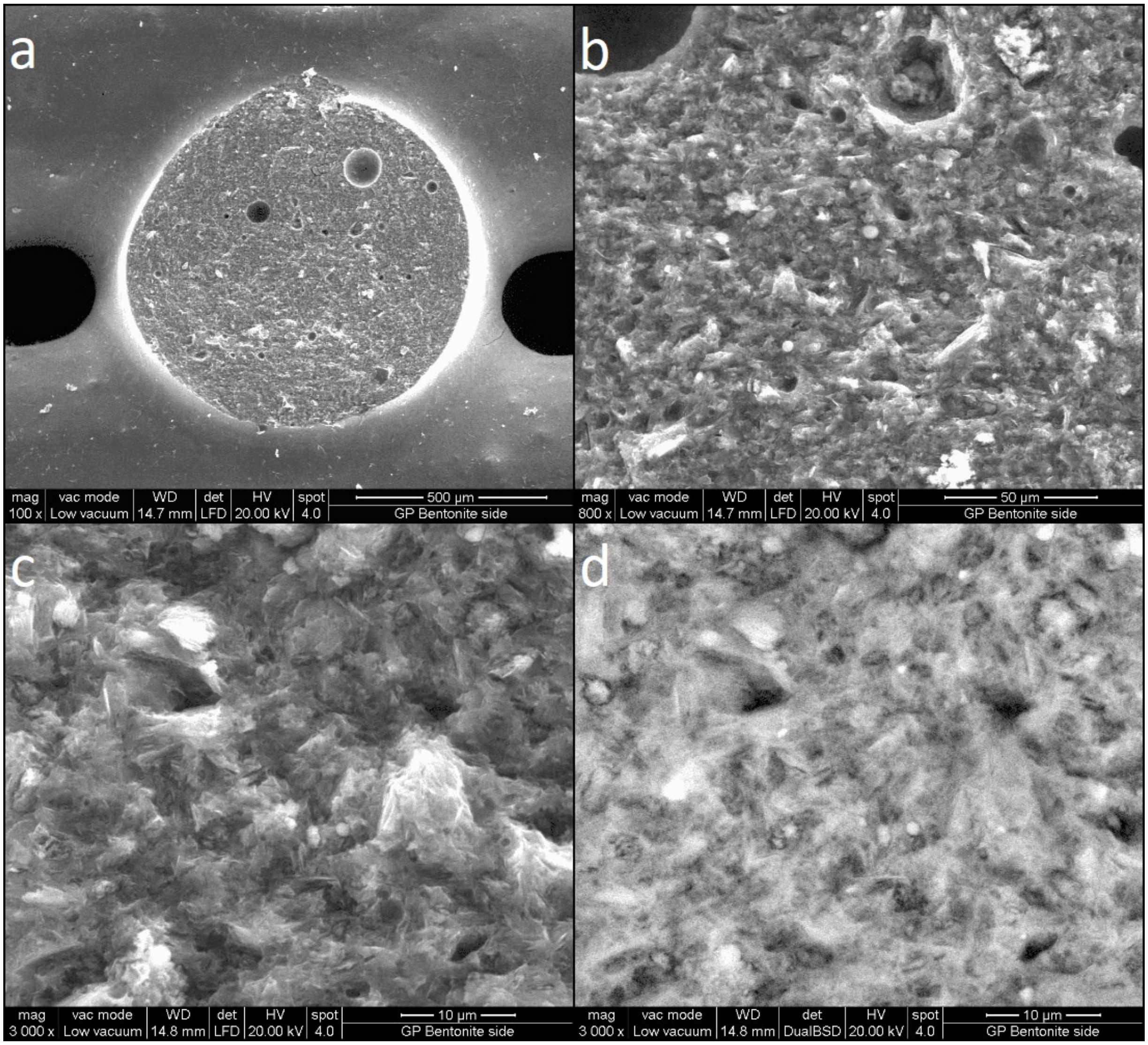

Figure 6.2: SEM micrographs for GP13 showing the fracture surface of a filament at 100x magnification (a), 800x magnification (b), 2000x magnification (c) with associated BSE mode (d).

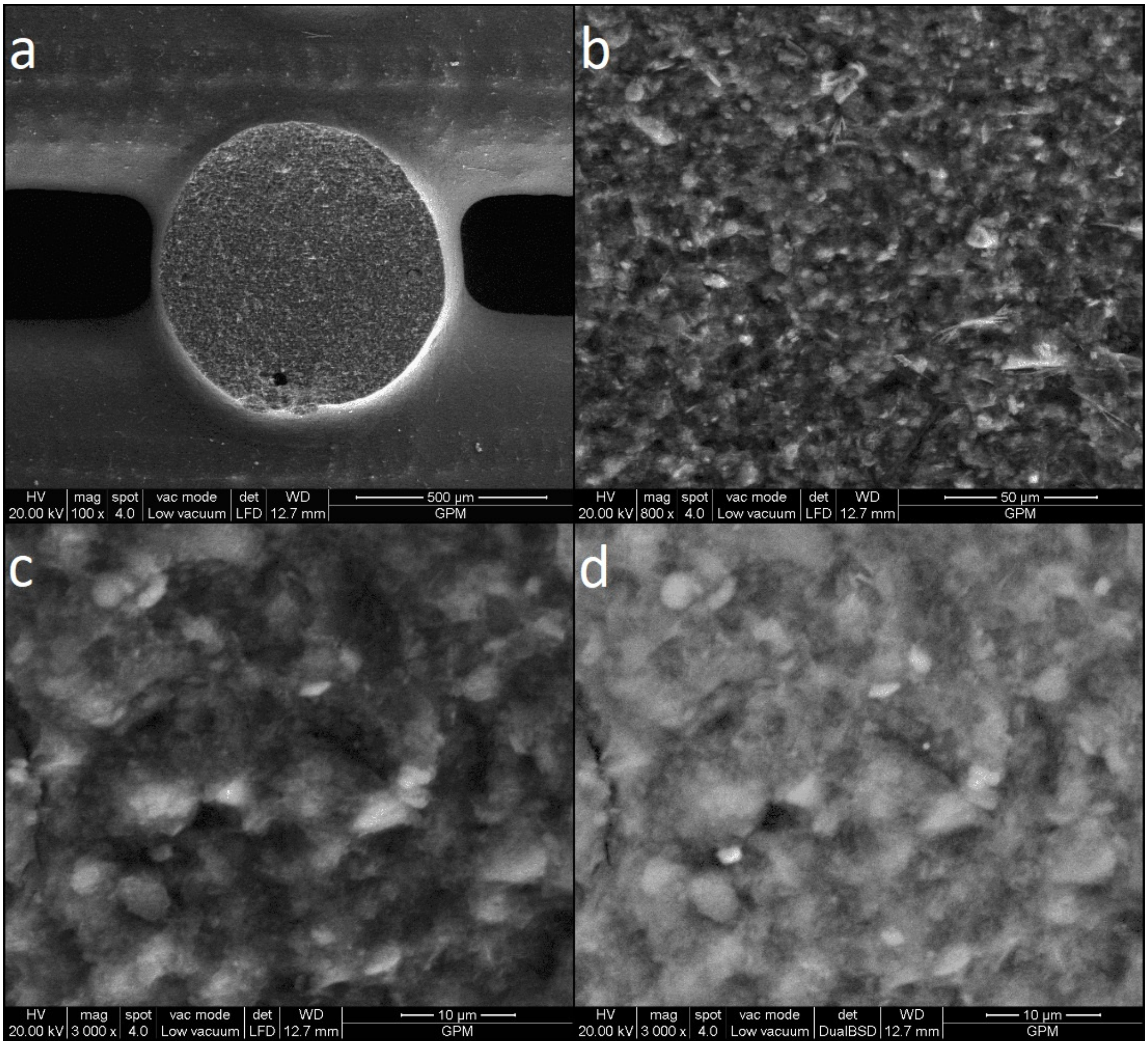

Figure 6.3: SEM micrographs for GP-MFI showing the fracture surface of a filament at 100x magnification (a), 800x magnification (b), 2000x magnification (c) with associated BSE mode (d).

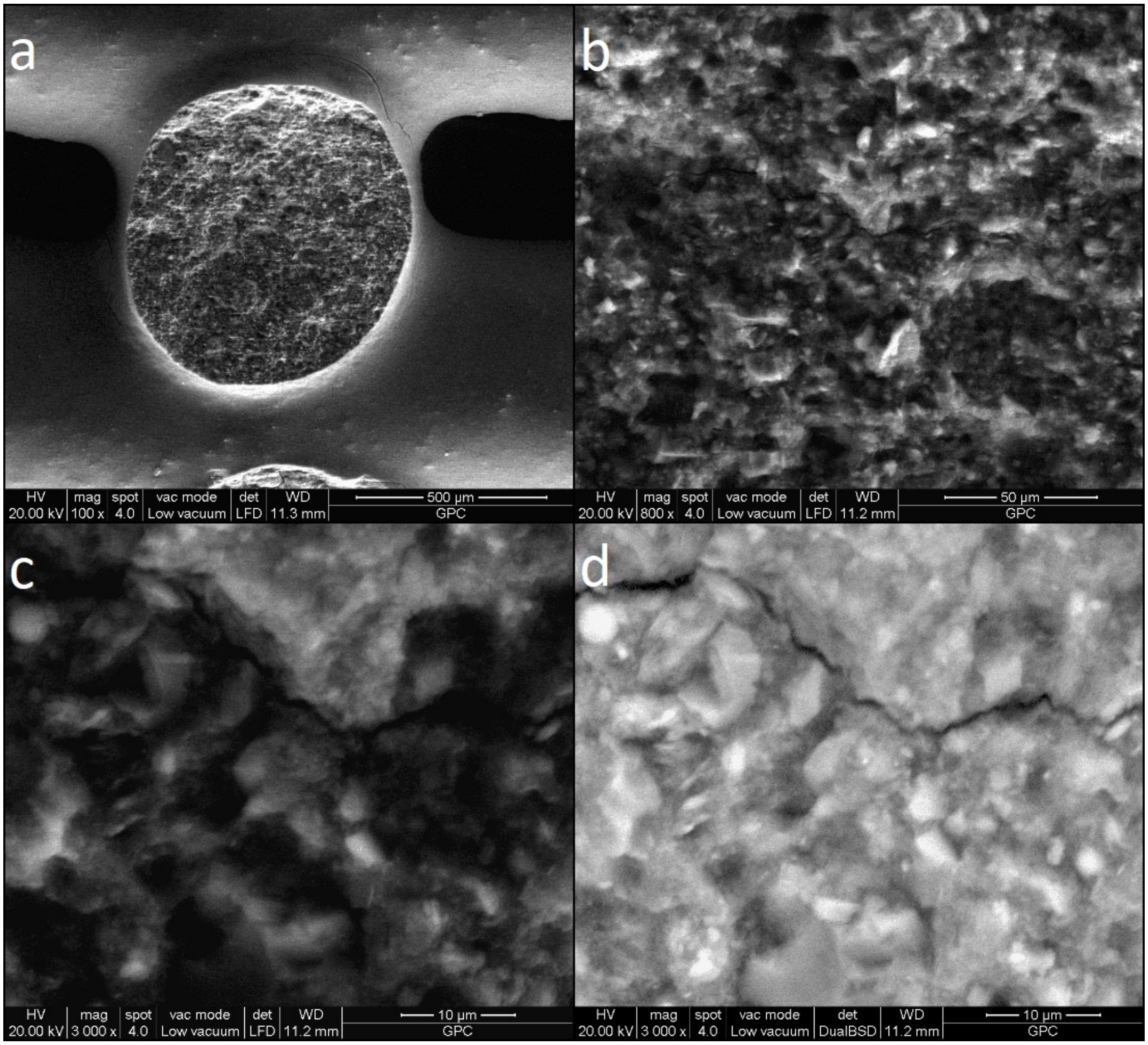

Figure 6.4: SEM micrographs for GP-CHA showing the fracture surface of a filament at 100x magnification (a), 800x magnification (b), 2000x magnification (c) with associated BSE mode (d).

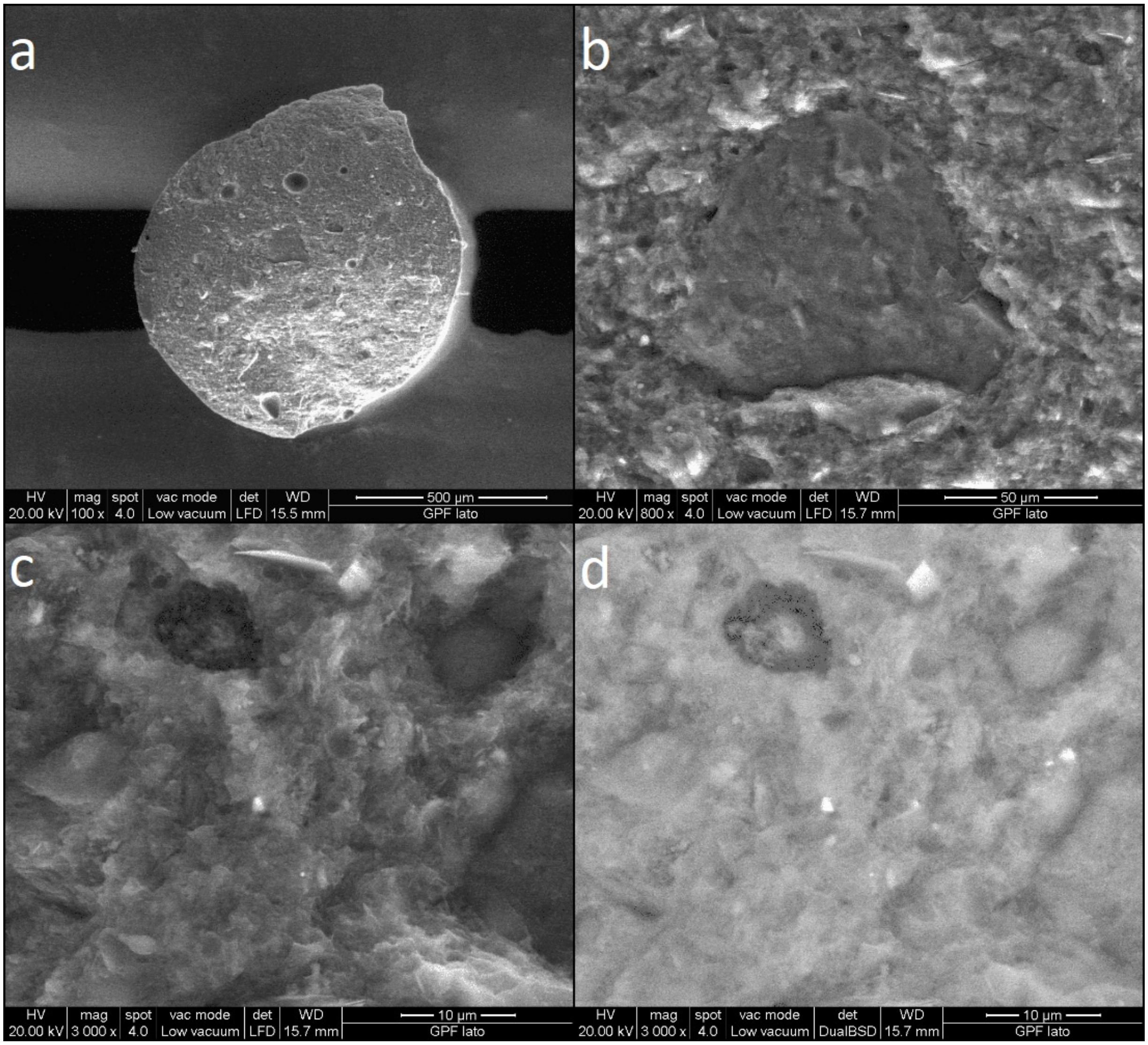

Figure 6.5: SEM micrographs for GP-FAU showing the fracture surface of a filament at 100x magnification (a), 800x magnification (b), 2000x magnification (c) with associated BSE mode (d).

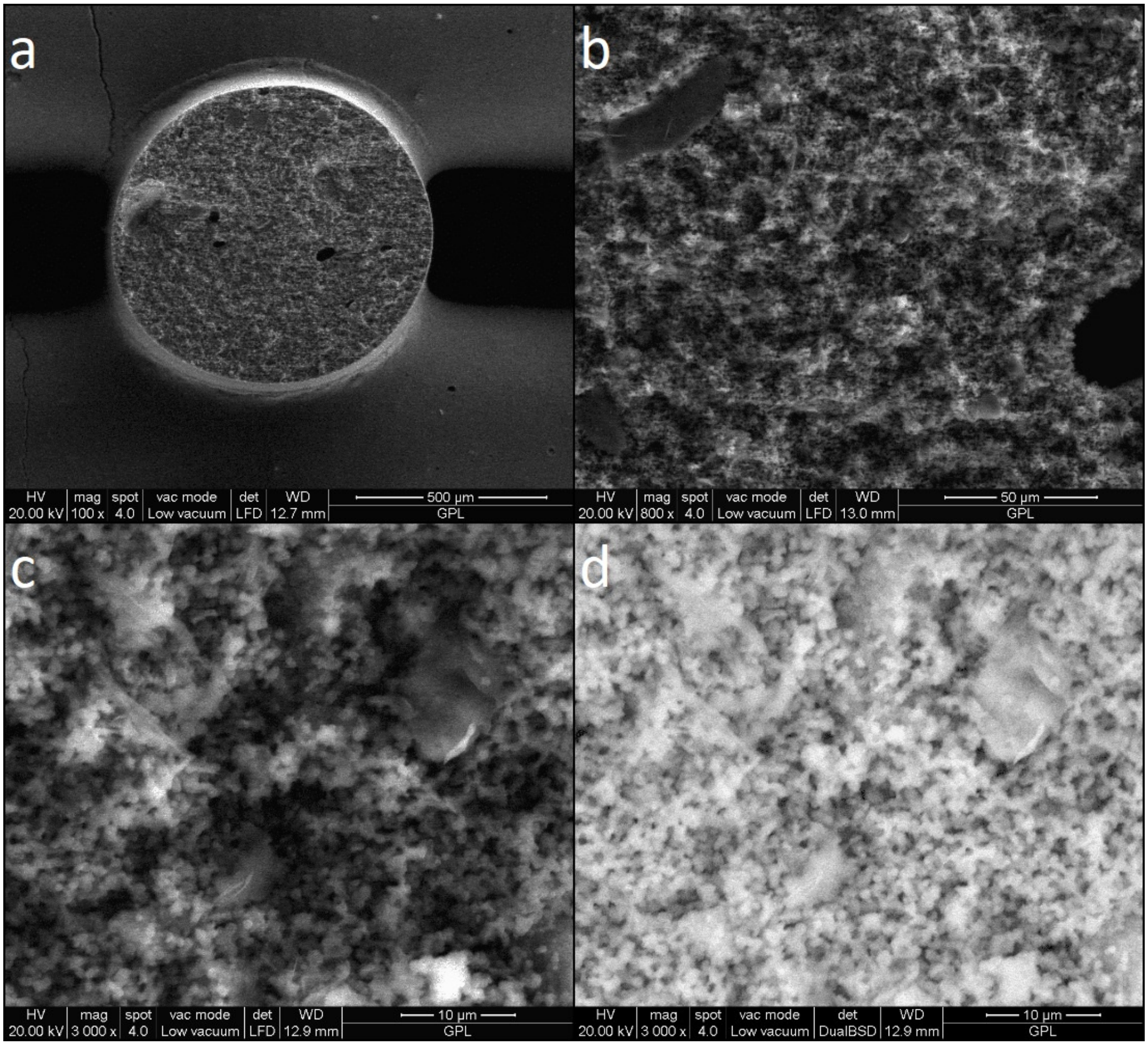

Figure 6.6: SEM micrographs for GP-LTA showing the fracture surface of a filament at 100x magnification (a), 800x magnification (b), 2000x magnification (c) with associated BSE mode (d).

Chapter 7

Structural characterisation

Chracterisation of the geopolymer inks by diffractometry is somewhat less insightful compared to the fillers due to the amorphous nature of the matrix. The very first stage of geopolymerisation, corresponding to the dissolution of reagents in the activating solution, requires the presence of reactive precursors which are invariably amorphous as the superior stability of crystalline constituents precludes their utilisation as oxide source. Thus, the overall reaction involves an amorphous-amorphous transition which is difficult to investigate by XRD. It can be seen from the experimental patterns for Argical and GP13 (Fig. 7.1.a) that the halo position shifts to higher angles indicating that the metakaolin structure is thoroughly transformed, but the crystalline impurities are essentially unaffected by the conversion and remain well visible in the geopolymer pattern. Such impurities were identified as α-quartz, anatase, muscovite and residual kaolinite left from the calcination treatment. Since chemical interactions between the matrix and fillers are assumed to be minimal and no crystalline phases should be consumed or produced during the conversion, diffractometry may be used to assess the stability of the geopolymer-zeolite systems especially in the MK-inks where the role of the matrix is purely mechanical. XRD patterns for GP-MFI and GP-CHA (Fig. 7.2) and GP-FAU (Fig. 7.3.a) measured after the 20 d curing period, confirm that the zeolites remain stable within the amorphous matrix and all crystalline peaks observed can be attributed to the filler or the crystalline MK impurities. GP-CHA and GP-FAU especially also display the characteristic bentonite peak complex at 20-30° (pattern presented in Fig. 7.1, owing to its more significant fraction in the composition of these two inks. In some cases measurements were repeated at months' distance without displaying any significant changes in the intensity of crystalline peaks: it was thus concluded that the geopolymer matrix poses no concern on the stability of the fillers.

In GP-LTA the use of diffractometry provides the additional advantage of characterising the formation of the secondary LTA fraction during curing. The primary filler was added to the aluminate ink in much higher fractions compared to the MK system (33% and ≈16% respectively) thanks to the superior stability of the suspension and with additional post-forming zeolitisation the composite was expected to achieve significant levels of crystallinity. In a preliminary assessment XRD was used to determine the best conditions to favour secondary crystallisation: GP-LTA samples were cured in sealed containers at room temperature (7 d), 40°C (4 d) and 75°C (3 d). The patterns, presented in Fig. 7.4.a, show that only the 75°C sample gave rise to enhanced peak intensity, while the other two were found to be comparable: it was thus concluded that for the room-temperature and 40°C samples the crystalline fraction remained essentially unchanged during curing. All peaks in the 75°C pattern were identified as LTA reflections as this particular ink was produced with a first version of the LTA filler which contained no zeolite P, however both the RT and 40°C specimens exhibited the presence of an unaccounted peak at ≈18° which is compatible with $Al(OH)_3$ (gibbsite): it is likely that the rapid water evaporation from the porous printed structures and reduced polycondensation rate at low temperature produced a supersaturated environment from which $Al(OH)_3$ precipitated before it could be completely immobilised within the geopolymer network.

Due to the necessity of validating the simultaneous curing-zeolitisation step, an attempt was made to quantify the final crystalline fraction of GP-LTA from diffraction data. The aluminate matrix (3.8-1-25 composition) was found to give rise to a purely amorphous structure when cured in open containers, thus providing an ideal background to its partially crystallised counterpart in GP-LTA. If the primary and secondary LTA zeolites are assumed to be equal in light of their similar precursor composition and growth conditions, then the final composite can be reasonably modelled as an equivalent mixture of amorphous aluminate geopolymer and LTA filler which results in the same diffraction intensity. A series of reference samples was prepared by combining powdered aluminate geopolymer with the same filler used in GP-LTA at various crystalline fractions and diffraction patterns were obtained in the 15-40° interval, comprising both the amorphous halo and some of the strongest LTA reflections (Fig. 7.4.b); the filler was assumed to all effects to have 100% crystallinity. Intensity of the five main LTA peaks (P_1-P_5) as well as the GIS peak (P_{GIS}) were plotted as function of filler fraction (Fig. 7.4.c); for the 0 wt.% sample, which has no crystalline peaks, the intensity at the appropriate 2θ value was considered instead. The experimental data was found to be well described by quadratic polynomials, whose parameters are given in Tab. 7.1. The measured GP-LTA intensity for each of the six peaks was then associated to its corresponding crystalline fraction according to the polynomial trend and the results found to be in remarkable agreement. All LTA peaks point to a crystalline fraction of 68-69 wt.%, with the only exception of P_3 resulting in a lower calculated 57 wt% value: this discrepancy is due to the fact that in the GP-LTA pattern P_3 was found to have lower intensity than P_4, despite the opposite being true for all the measured reference patterns. Discounting an effect of preferential orientation, which seems unlikely given the isotropic nature of LTA crystals and close similarities between GP-LTA and the reference powders, the discrepancy was assumed to arise simply from experimental error during collection of the GP-LTA pattern. The average crystalline fraction, as calculated from the combined results of the five LTA peaks, is 66 ± 5 wt.% which is validated even without relying on the fitting polynomials by virtue of the experimental intensities clearly falling between those of the 60 wt.% and 70 wt.% references, towards the upper limit of the interval. The huge difference with the GIS peak, which produces a calculated crystallinity of 25 wt%, would appear to indicate that secondary crystallisation during curing involves the predominant formation of LTA with respect to GIS, an effect which is likely enhanced through seeding by the primary filler particles.

Table 7.1: Polynomial regression parameters and R^2 values for the evolution of peak intensity with filler fraction according to $y = ax^2 + bx + c$; the experimental GP-LTA intensities (I_{exp}) as well as their corresponding crystalline fractions (X_{calc}) calculated using the fit equations are also presented here.

Peak	**Main reflection**	**a**	**b**	**c**	**R2**	**I_{exp} (a.u.)**	**X_{calc} (%)**
P_1	LTA {8 2 0}	-1.82	753.28	7542.12	0.9971	50581	68.43
P_2	LTA {6 2 2}	-1.79	691.86	8732.26	0.9981	47807	68.64
P_3	LTA {4 4 2}	-1.68	649.26	8956.13	0.9968	40390	56.76
P_4	LTA {6 4 2}	-1.62	591.55	8283.87	0.9962	41319	68.87
P_5	LTA {6 6 4}	-0.85	413.01	5634.07	0.9975	29918	68.46
P_{GIS}	GIS {3 1 0}	-0.76	224.49	8976.69	0.9936	14103	24.93

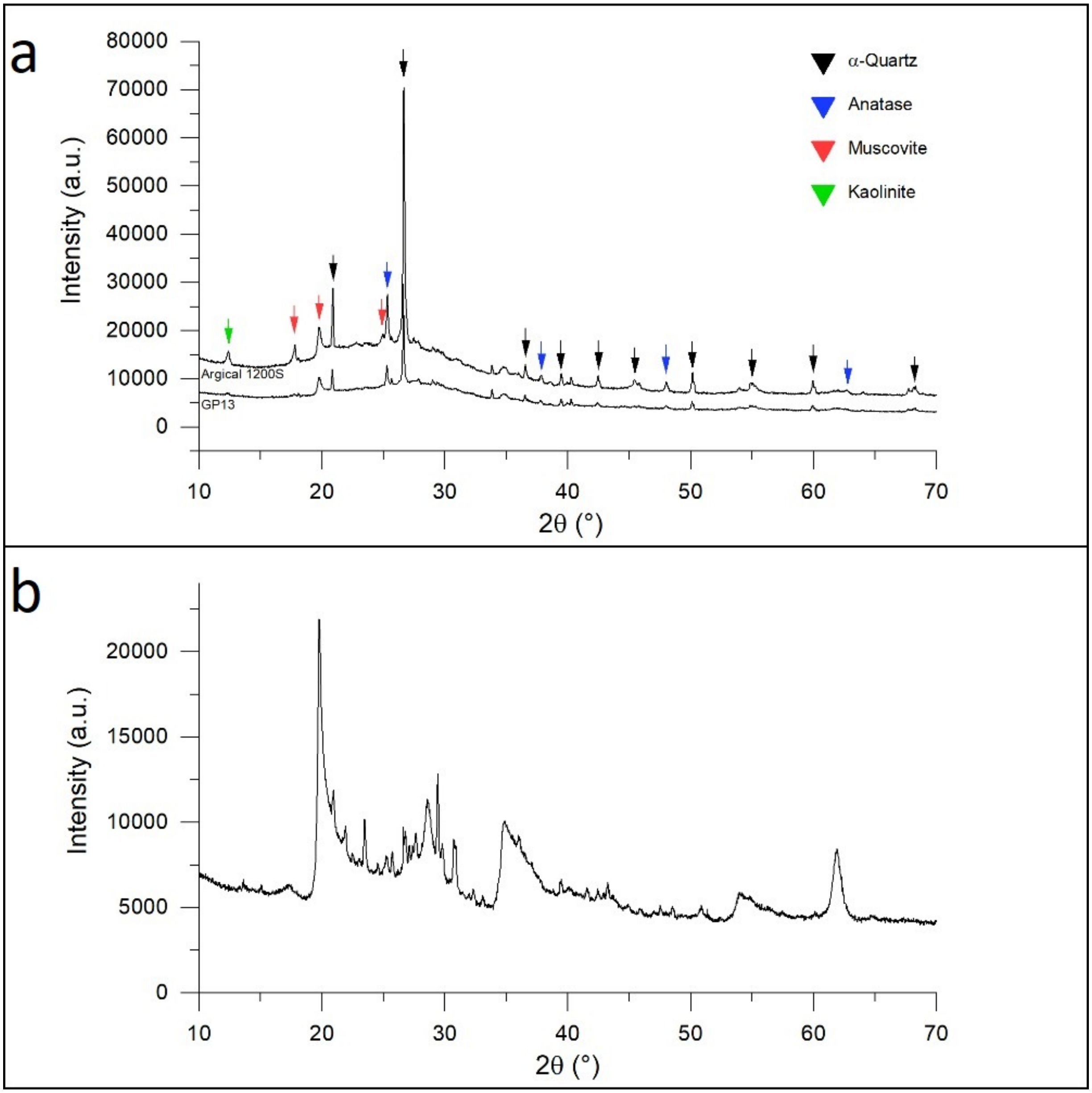

Figure 7.1: Comparison of XRD patterns for Argical 1200S and GP13 showing the presence of identical crystalline impurities (a) and pattern for bentonite (b); collected with CuKα radiation, 0.02° step size and 0.6°/min scan speed.

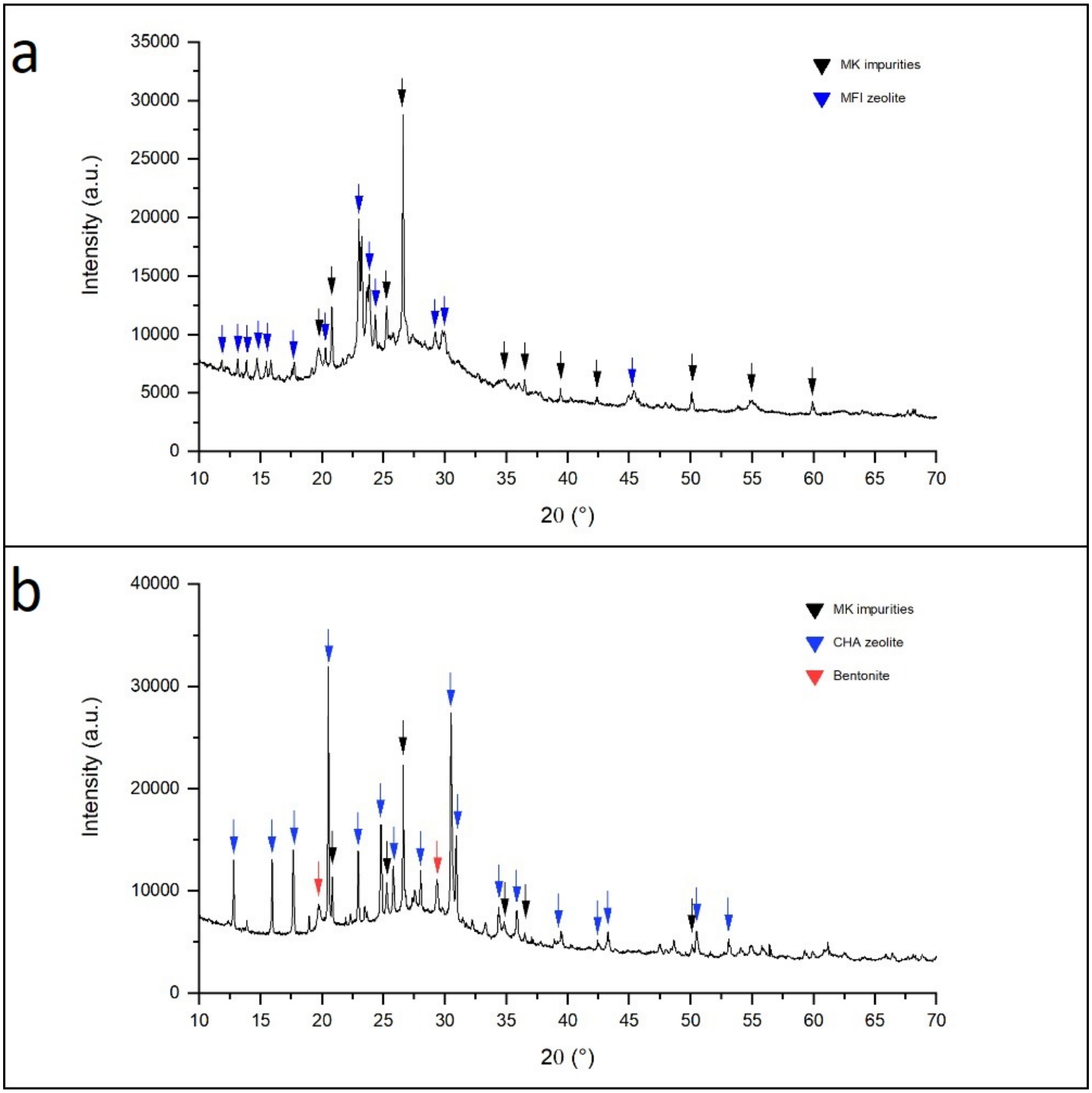

Figure 7.2: Diffraction patterns for GP-MFI (a) and GP-CHA (b); collected with CuKα radiation, 0.02° step size and 0.6°/min scan speed.

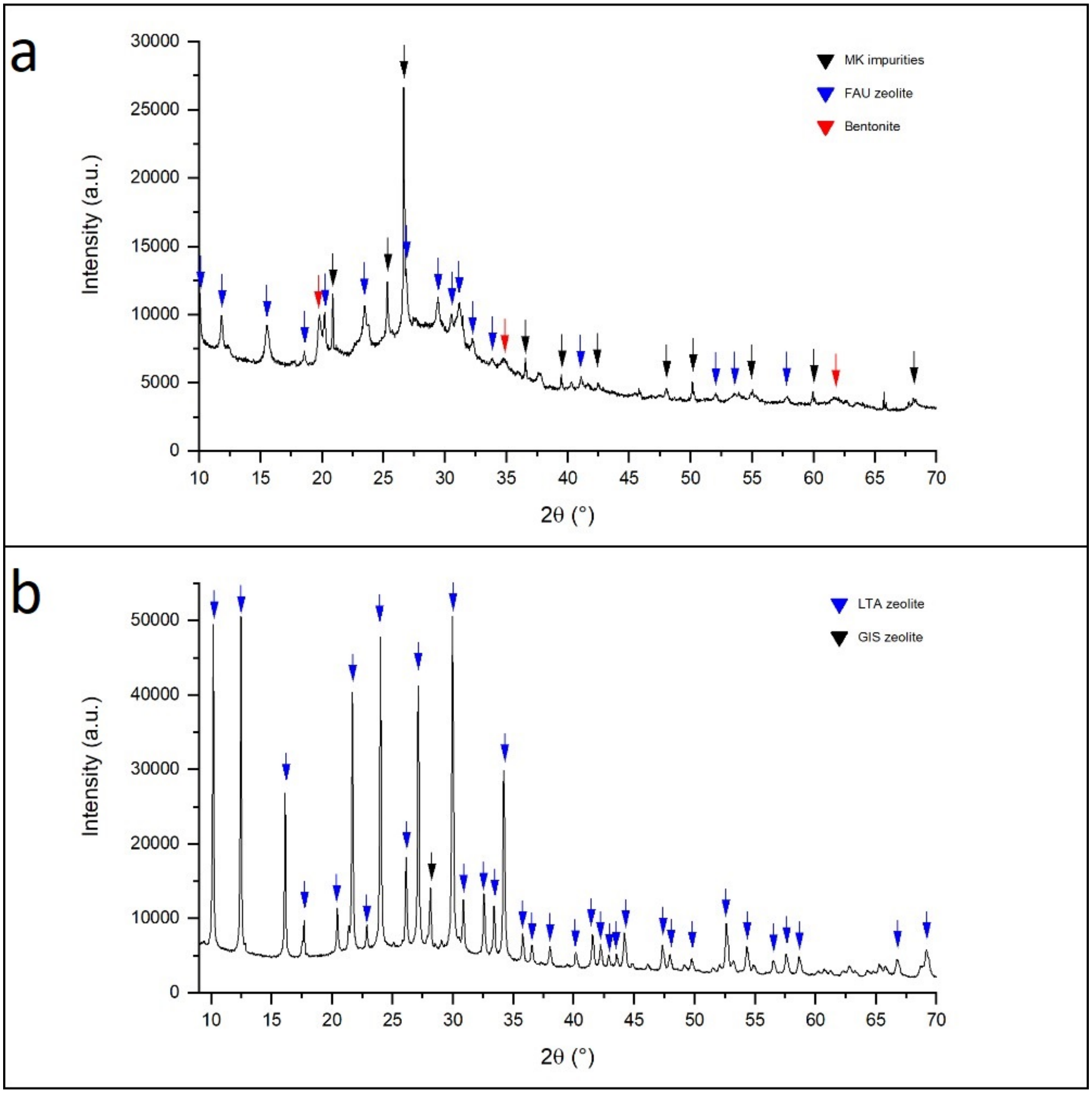

Figure 7.3: Diffraction patterns for GP-FAU (a) and GP-LTA (b); collected with CuKα radiation, 0.02° step size and 0.6°/min scan speed.

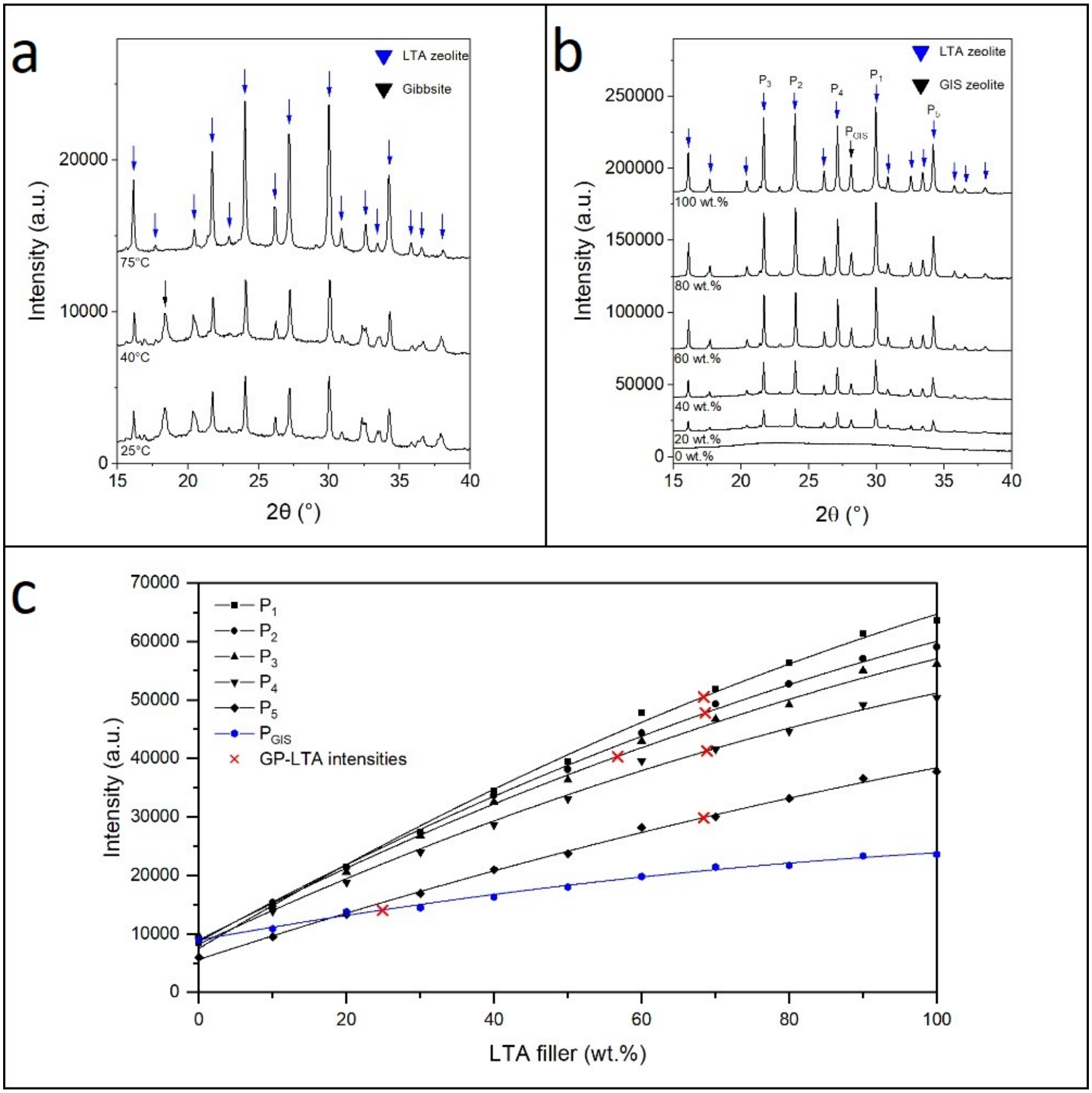

Figure 7.4: Diffraction patterns for GP-LTA cured at different temperatures (a) and selected reference patterns collected from amorphous-LTA systems with different crystalline fractions (b); experimental data and polynomial regression of peak intensities with increasing fraction of LTA filler (c), red crosses denote experimental intensities of GP-LTA placed at their corresponding calculated crystallinity.

Chapter 8

Mechanical characterisation

The proposed application of the monoliths as natural gas desiccants somewhat puts their mechanical performance on a lower priority compared to surface area and moisture adsorption capabilities. Strictly speaking, if the components are strong enough to be handled during manufacturing and transportation then it is unlikely that issues might arise from the weak mechanical loads experienced from gas streams during service. It is however important to investigate the weakening effects of filler addition to the matrix, as the nucleation of zeolites during geopolymer ageing has been reported to cause a slight reduction of the mechanical properties. Moreover, a compromise between strength and surface area must be found: mesoporosity, originating from the evaporation of water in the gel network, also results in a less dense and overall weaker structure.[30]

Compression tests were carried out for the S90 specimens on a hydraulic press equipped with a 10 kN load cell (Instron, 1121 series), at 0.5 mm/min. Before testing the monoliths were lightly ground on each side on a 120 μm diamond wheel in order to obtain smooth surfaces for easier measurement and homogeneous grip by the compression apparatus. The number of samples for each material varied, as it was preferred to test monoliths coming from a single printing session for higher reliability: in any case, at least ten specimens per material were analysed to ensure accurate results. Brittle failure in ceramics is dominated by the presence of defects from processing steps, which act as crack initiation sites for rapid fracture once their critical stress is exceeded: this ”weakest-link” mechanism results in a non-normal distribution of experimental strength values which must be characterised through a probabilistic approach. The most commonly used model in ceramic failure analysis is the two-parameter Weibull distribution, which can be expressed by:[37]

$$S = exp\left[-\left(\frac{\sigma}{\sigma_0}\right)^m\right] \tag{8.1}$$

Eqn. 8.1 describes the cumulative survival probability (S) of a brittle sample when subjected to a certain mechanical stress σ. The distribution is characterised by two parameters, m and σ_0, which are experimentally determined. The shape factor m, more commonly known as Weibull modulus, describes the slope of the curve in the descending branch: high values of m, typical for metals, indicate that the distribution of failure stresses is narrow and thus a single average value may be used to characterise it. On the other hand σ_0, also called scale factor, represents the stress at which survival probability is equal to 1/e ($\approx$ 37%). Eqn 8.1 may also be expressed in linear form by rearranging its terms:

$$ln\left[ln\left(\frac{1}{S}\right)\right] = mln(\sigma) - mln(\sigma_0) \tag{8.2}$$

In this case a plot of $ln\left[ln\left(\frac{1}{S}\right)\right]$ against $ln(\sigma)$ yields a straight line with slope and intercept equal to m and $mln(\sigma_0)$ respectively, thus allowing for experimental determination of the two parameters. A common estimator for the cumulative survival probability of the j^{th} specimen among a population of N (sorted by ascending fracture stress) is given by:

$$S' = \frac{j - 0.5}{N} \tag{8.3}$$

The survival probability is given in this case as S' because it must be further corrected for the volume of the samples: since failure is governed by the statistical nature of defects, larger volumes imply a higher probability of harbouring a critical defects which may cause crack initiation. Thus, if the specimens used for the compression test campaign are not nominally equal to a reference volume V_0, it is expected that S' must be increased for samples with $V<V_0$ and decreased otherwise according to:

$$S = S'^{\left(\frac{V}{V_0}\right)} \tag{8.4}$$

Once all the S-σ couples have been calculated the data can finally be plotted following Eqn. 8.2 to extract the Weibull parameters.

A comparison of Weibull plots for the five samples is presented in Fig. 8.1 both in linear and exponential form, while raw values for Weibull modelling of all samples can be found in Appendix A. It can be seen that the addition of zeolites to the geopolymer matrix resulted in a reduction of mechanical properties as expected from literature, however such effect appears to be almost independent of filler type with all zeolitic inks performing quite similarly compared to GP13. GP-FAU exhibited the most significant variation, with a substantial reduction of the Weibull modulus as seen in Tab. 8.1: this might be related to the wide size distribution of the FAU powder potentially resulting in a less homogeneous structure compared to the others. The lower mechanical performance may contribute to explain why heat-treatments cracks were only observed in GP-FAU and none of the other samples, as discussed in Chapter 6. This contribution from powder morphology is supported by the relative performances of the other filled inks, with the highly homogeneous MFI ranking first followed by LTA.

Table 8.1: Summary of sample size and Weibull parameters, with calculated stresses for 90%, 99% and 99.9% survival probability

Sample	**N**	**m**	σ_0 **(MPa)**	$\sigma_{90\%}$ **(MPa)**	$\sigma_{99\%}$ **(MPa)**	$\sigma_{99.9\%}$ **(MPa)**
GP13	10	6.04	9.82	6.77	4.59	3.13
GP-MFI	17	5.93	6.61	4.53	3.05	2.06
GP-CHA	18	6.44	4.83	3.41	2.36	1.65
GP-FAU	17	4.07	4.83	2.78	1.56	0.89
GP-LTA	12	5.72	5.98	4.04	2.68	1.79

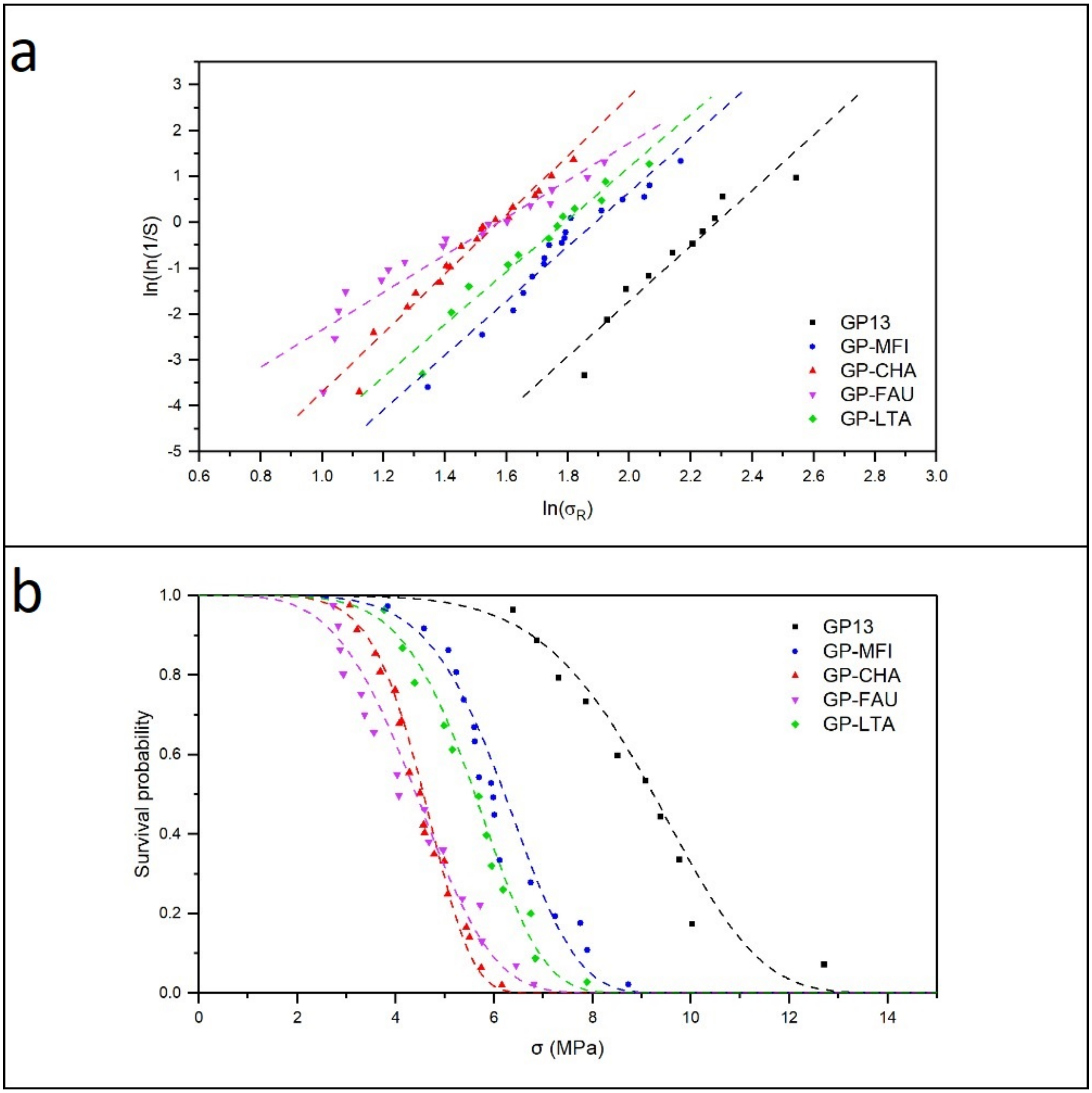

Figure 8.1: Linear regression (a) and Weibull plots (b) from compression testing of the five samples

Chapter 9

Functional characterisation

The characterisation of porosity and specific surface area are of paramount importance in the design of catalysts and adsorbents. Indeed, the aim of this study is to exploit DIW and the intrinsically porous structures of geopolymers and zeolites to obtain adsorbents with hierarchical porosity on several scales. Investigation of such structure is complicated by the variety of morphologies and formation mechanisms which it involves, in particular:

- Geometrical porosity ($\approx$ 1 mm) which concerns the design of the lattice
- Closed porosity ($\approx$ 100 μm) caused by air bubbles trapped within the filaments, as seen in Fig. 6.2.2.a; such porosity is inaccessible from the surface and thus undesired
- Mesoporosity ($\approx$ 2-50 nm), typical of geopolymers, formed by the evaporation of water from the gel network during polycondensation
- Ordered microporosity ($<$ 2 nm) of zeolites

Geometrical porosity can be estimated from the CAD model by taking a representative ”unit cell” of the structure and calculating the ratio with the extruded filament volume. Such cell may be alternatively centred on a filament or pore, but ultimately it can be easily seen that for a beam lattice with 1.6 mm horizontal period and 0.6 layer height a total 1.6 mm filament length is extruded over a 1.6x1.6x0.6 mm cell. Thus, geometrical porosity can be calculated from a 0.8 mm filament diameter to be 47.67%.

Macroporosity can also be estimated from density measurements. In this case density for all samples was measured on the bulk lattice (ρ_B), on fragments from the compression test (ρ_A) and on powders sieved at 125 μm (ρ_T). The total (P$_T$) and open porosity (P$_O$) can then be calculated from these values according to:

$$P_T = 1 - \frac{\rho_B}{\rho_T} \tag{9.1}$$

$$P_O = 1 - \frac{\rho_B}{\rho_A} \tag{9.2}$$

Bulk density was calculated from the mass and external volume of the lattices before compression testing, while apparent and true porosity measured from fragments and 125 μm powder through helium pycnometry. A summary of the results is displayed in Tab. 9.1.1 together with the calculated porosities; standard deviation is 0.01 g cm^{-3} for ρ_A and ρ_T and 0.03 g cm^{-3} for ρ_B owing to the greater variability of the printed lattices. It can be seen that P$_T$ is much higher than the 48% value which was calculated earlier: this is due to the fact that during printing various phenomena such as trapped bubbles or poor adhesion to the underlying layer can result in localised fragmentation of the filament with reduction of the total extruded volume, while the opposite only occurs if air pressure or flow parameters greatly exceed the ideal values. All samples present extremely limited closed porosity when compared to the total value, with P$_O$ and P$_T$ in close agreement: in the case of GP13 the calculated P$_T$ appears to be even lower than P$_O$, although this is obviously an artefact of ρ_A and ρ_T being within the range of standard deviation.

Table 9.1: Measured bulk, apparent and true density for the samples with calculated open and total porosity

Sample	ρ_B **(g cm^{-3})**	ρ_A **(g cm^{-3})**	ρ_T **(g cm^{-3})**	**P$_O$ (%)**	**P$_T$ (%)**
GP13	0.85	2.23	2.22	61.92	61.77
GP-MFI	0.76	2.09	2.10	63.60	63.71
GP-CHA	0.77	2.12	2.15	63.56	64.11
GP-FAU	0.72	2.09	2.10	65.77	65.87
GP-LTA	0.74	2.09	2.11	64.83	65.03

Brunauer-Emmet-Teller (BET) theory is a model for the multilayer physisorption of gas molecules on solid surfaces which is most commonly used for quantification of specific surface area. It predicts that multimolecular adsorption isotherms may be described by:

$$\frac{p}{v(p_0 - p)} = \frac{1}{v_m c} + \frac{c-1}{v_m c}\frac{p}{p_0} \tag{9.3}$$

where v represents the adsorbed volume at a specific pressure p lower than the vapour pressure p_0, v_m the volume of monolayer-adsorbed gas and c a parameter which is exponentially related to the difference between the monolayer heat of adsorption and the heat of liquefaction of the gas. By plotting $p/v(p_0 - p)$ against p/p_0 yields a straight line where v_m and c can be estimated from the slope and intercept and thus, by knowing the v and the cross-section of the adsorbate module, allow calculation of the surface area of the sample. The shape of the isotherm is related to adsorbate-surface and adsorbate-adsorbate interaction mechanisms.[5]

BET was first and foremost used to validate the use of bentonite as printing additive. The inclusion of hydrophilic polymers such as poly-ehtylene glycol (PEG) and carboxy methyl cellulose (CMC) in geopolymeric slurries has been reported to have marked positive effects on the rheology and mechanical properties of the condensed aluminosilicates.[10] Such organic additives, however, have poor stability at the higher temperatures which are required for service and regeneration in separation and catalysis applications. The carbonaceous residues left behind by pyrolisation of PEG are thought to result in a reduction of porosity and specific surface area which constitutes a significant concern. Bentonite on the other hand remains stable within the matrix due to its inorganic nature and high chemical affinity, which allows for post-processing of printed geopolymers to be performed entirely at room temperature.

In order to evaluate the differences between PEG and bentonite, as well as the effect of DIW on the surface area, BET was performed on four samples of composition $3.8SiO_2$-Na_2O-Al_2O_3-$13H_2O$ with different additives and processing routes: the first geopolymer (GP) was simply cast with no additives, while GP-PEG and GP13-F were analysed as fragments from printed lattices using PEG and bentonite. A fourth sample, GP13-P was prepared in powdered form from GP13-F; both were obtained from the GP13 lattices, while GP-PEG was supplied from a previous research project in the department. Curing had been carried out at 75°C for two days in sealed containers in all cases. BET surface areas are presented in Tab. 9.2 together with a brief description of the materials analysed. It can be seen that the addition of PEG results in a substantial reduction of SSA with respect to the cast geopolymer, while for GP13-F the effect, although still present, is considerably less pronounced. The printing process however appears to play a significant role in the reduction of surface area as evidenced by the powdered specimen GP13-P: it is possible that extrusion through the nozzle places the outer layer of the struts in a state of compression which might result in the formation of a densified skin around a more porous structure. Such effect was observed during SEM of some of the filled samples, most notably GP-FAU, where in selected points it appeared that a section of the "skin" had peeled off revealing a considerably more macroporous structure. It is unclear, however, whether the same can be applied to to the lower-scale mesoporosity which is expected in geopolymeric materials. N_2 isotherms for all four samples, presented in Fig. 9.1, can be ascribed to Type IV with the presence of additional macropores which cause the rapid increase of adsorption close to p/p_0=1; the H3-type hysteresis loop is associated to condensation of the adsorbate gas within tortuous and interconnected mesopores with a slit-shaped geometry which is most common for aggregates of plate-like structures.[35] The hysteresis is more pronounced in GP compared to the printed samples, which might indicate an additional effect of DIW on the formation of mesopores possibly associated with the faster evaporation of water from the open structure during curing.

Table 9.2: BET surface area for 3.8SiO_2-Na_2O-Al_2O_3-13H_2O MK-geopolymers with different additives and forming processes

Sample	**Notes**	**BET surface area (m^2 g^{-1})**
GP	Cast, no additives	18.29
GP-PEG	Printed with PEG, fragments	3.71
GP13-F	Printed with bentonite, fragments	11.94
GP13-P	Printed with bentonite, powder	16.26

Isotherms for the filled samples are also reported (Fig. 9.2). In this case the mesopore hysteresis persists, but it appears less significant and even almost non-exixtent in the case of GP-LTA. The knee region at low p/p_0 is associated with monolayer formation inside micropores, which are obviously present in these samples thanks to the addition of zeolites. The BET SSA values, presented in Tab. 9.3, show that filler addition has a remarkable positive effect on all MK-based composites compared to the unfilled material: the general rank is the same observed for the TGA-derived water adsorption of zeolites with GP-FAU emerging as the clear winner. The abysmal result of GP-LTA on the other hand was entirely unexpected based on TGA and the high crystallinity characterised through XRD, since no explanation could be found regarding the filler it must be concluded that the aluminate matrix does not possess the tortuous and interconnected pore structure typical of MK-geopolymers thus greatly reducing the fraction of LTA surface area exposed to the adsorbate, or that the use of a colloidal system allows the geopolymer to fully enclose the filler during printing and occlude microporosity. This is cleary of great concern in the present study, as the SSA of GP-LTA (even lower than GP-PEG) essentially makes it an unviable candidate.

The BJH pore size curves (Fig. 9.3) for the unfilled samples show a bimodal distribution in mesoporosity with two peaks close to the limiting values of the interval (2 nm and 50 nm), however only GP clearly shows distribution peaks well within the range at 3 nm and 10 nm. For the

Table 9.3: BET surface area for the geopolymer-zeolite composites

Sample	**Notes**	**BET surface area ($\mathbf{m^2\ g^{-1}}$)**
GP-MFI		92.05
GP-CHA		114.54
GP-FAU		129.47
GP-LTA	Aluminate matrix	1.89

others they instead seem shifted to the micro- and macroporosity regions, which helps to explain the reduced hysterisis observed in the isotherms. Since the trend is similar for all printed samples, it would appear that the process, and not the additive, induces a partial suppression of the formation of mesopores in favour of macropores: although the mechanism is unclear the most striking difference between the two processing routes is the resulting macro-scale porosity which allows for faster water evaporation during curing. It is possible that moisture removal in the first stages of polycondensation leads to a partial collapse of the void system and consequently densification. Partial confirmation may be given by the fact that the composites, which were cured at room temperature and whose matrix has a higher water-to-filler ratio, show clear spikes in distribution for pores with 20-30 nm width. The microporous fraction, although outside of the scope of BJH theory, appears to be significant for all samples but is especially predominant with respect to the mesopores in GP-LTA. On the other hand, GP-FAU presents the opposite trend which may stem from the partially geopolymeric nature of the filler.

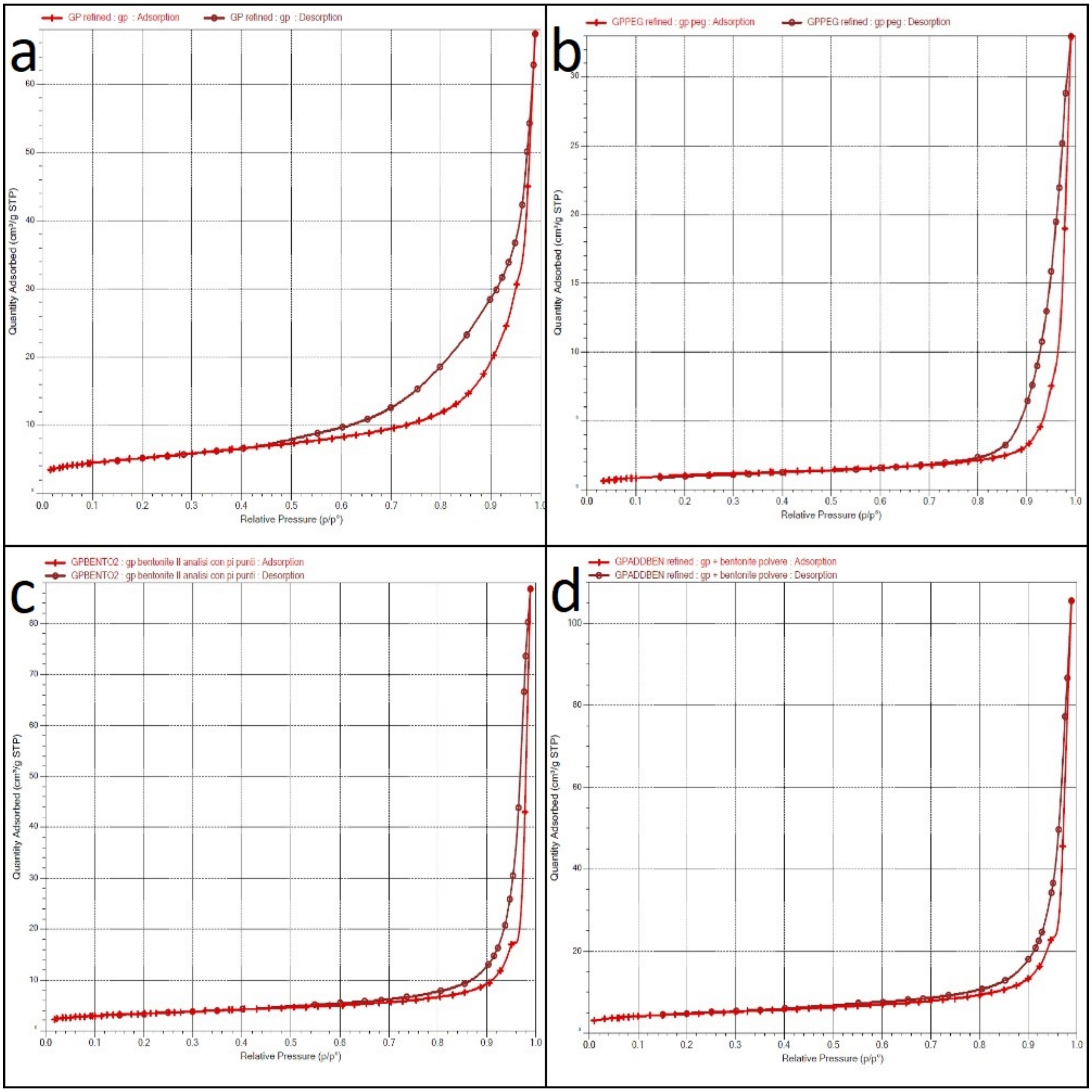

Figure 9.1: N_2 adsorption-desorption isotherms for the unfilled geopolymer samples: GP (a), GP-PEG (b), GP13-F (c) and GP13-P (d).

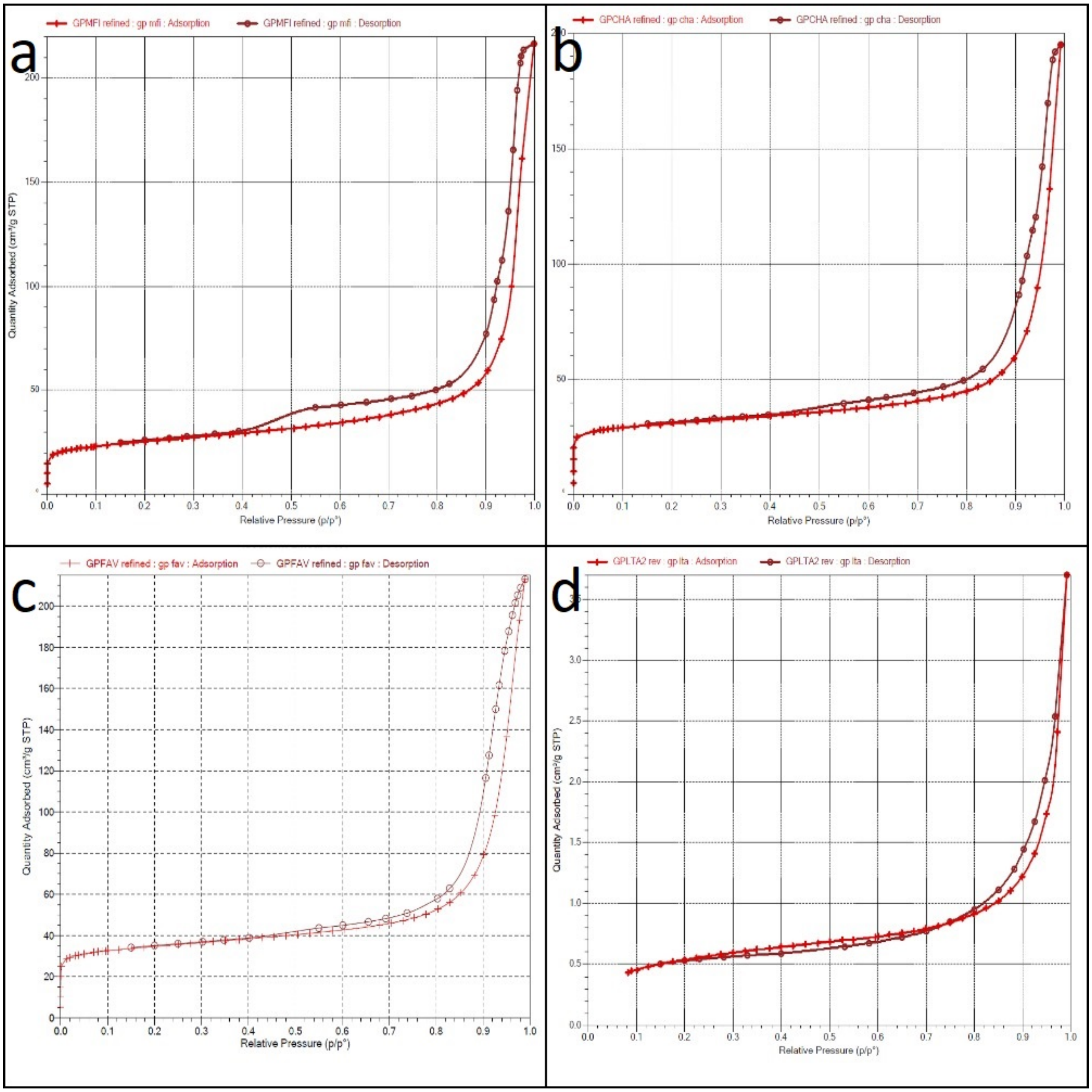

Figure 9.2: N_2 adsorption-desorption isotherms for the geopolymer-zeolite composites: GP-MFI (a), GP-CHA (b), GP-FAU (c) and GP-LTA (d).

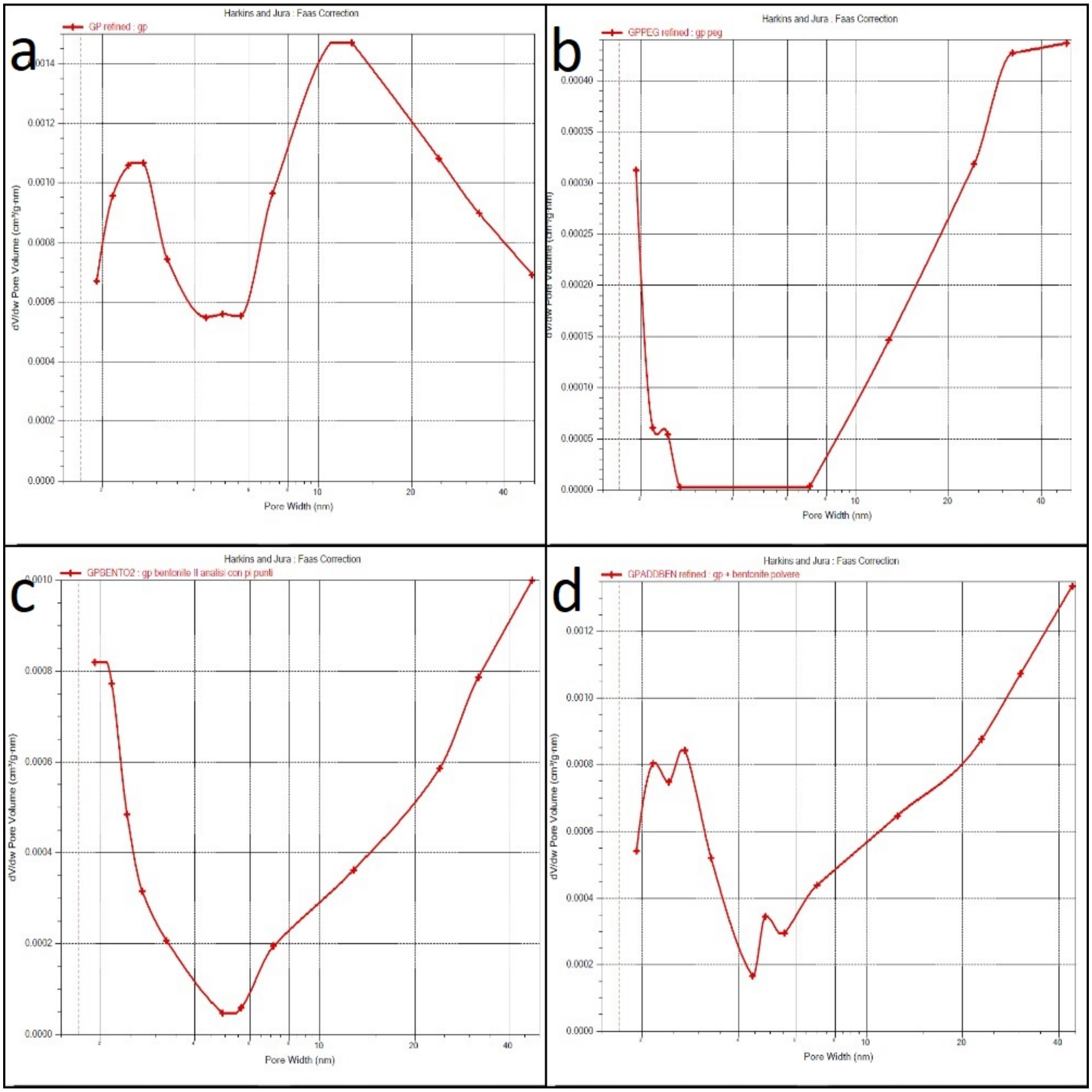

Figure 9.3: BJH differential pore volume distribution from the unfilled geopolymer samples: GP (a), GP-PEG (b), GP13-F (c) and GP13-P (d).

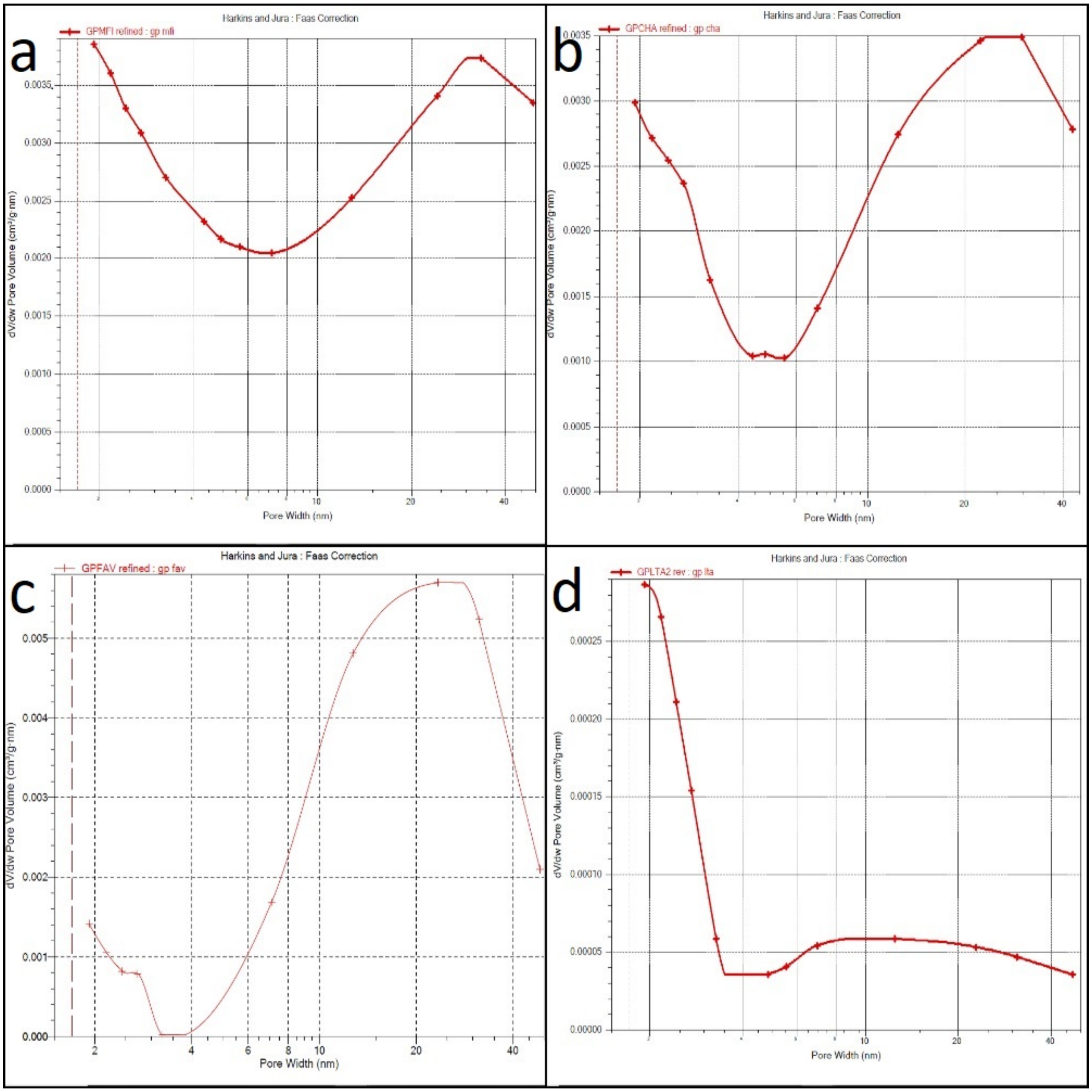

Figure 9.4: BJH differential pore volume distribution from the geopolymer-zeolite composites: GP-MFI (a), GP-CHA (b), GP-FAU (c) and GP-LTA (d).

Chapter 10

Proof-of-concept for 3D-printed adsorbents

The choice of S90 as a primary design for the monoliths was dictated by the necessity of rapidly printing several samples for use in compression testing, however its straight-channel structure is ill-suited for applications in separation and catalysis. Ideally porosity should be tortuous to allow for more contact between the reagents and the surface of the adsorbent, but the reduction in permeability should be kept to a minimum to avoid excessive pressurisation costs. C90 was thus designed to have an open and interconnected void fraction with twisted channels, the idea being that the gases are forced to follow a helical path around the z-axis increasing their permanence time without severely decreasing permeability.

Laminar fluid flow in porous media[27] can be described by Darcy's law according to:

$$\frac{\Delta P}{L} = \frac{\mu}{k_1} v_s \tag{10.1}$$

The pressure drop ΔP over a length L is proportional to the fluid velocity v_s through the dynamic viscosity, μ, and the permeability of the porous medium k_1. At high velocities the equation must be corrected for the inertial effects of turbulent flow, which gives Forchheimer's equation:

$$\frac{\Delta P}{L} = \frac{\mu}{k_1} v_s + \frac{\rho}{k_2} v_s^2 \tag{10.2}$$

where ρ is the fluid density and k_2 the inertial permeability. Moreover for compressible flow the pressure drop is given by:

$$\Delta P = \frac{P_{in}^2 - P_{out}^2}{2P_{out}} \tag{10.3}$$

Thus, by measuring ΔP through a porous medium over a range of fluid velocities a polynomial regression can be performed to determine the two structure-dependent permeability coefficients.[14] The $\Delta P/L$ against v_s trend for three C90 specimens is presented in Fig. 10.1.a. The correlation can indeed be described by a quadratic expression and the k_1 and k_2 terms were determined to equal $5.64 \pm 0.4 \cdot 10^{-9}$ m^2 and $2.62 \pm 0.2 \cdot 10^{-4}$ m. As shown in Fig. 10.1.b, these values place C90 on the high end of granular beds which are generally used for gas desiccation and close to the performance of honeycomb structures, where however flow is predominantly linear. The results of permeability tests prove that even with a non-optimised geometry printed lattices can have remarkably high performance compared to current commercial solutions.

The structure was also evaluated through X-ray microtomography to assess whether the design and geometrical tolerances had been maintained through printing and curing. The reconstructed CAD (Fig. 10.2.a, voxel size 26 μm) shows that the designed channel system remained well open throughout the print maintaining its fully interconnected nature. The sample also presented a low degree of closed porosity (0.13%) which is compatible with the calculated value from density measurements. Such voids have a homogeneous spatial distribution (Fig. 10.2.b) and analysis reveals that they are mostly spheroidal in shape. The size distribution (Fig. 10.2.c) presents a distinct maximum at around 120 μm: this is expected, as closed pores are caused by the presence of air bubbles in the ink and thus can only remain internal if their dimensions are much lower than the diameter of the filament (840 μm). The reconstructed CAD revealed that some volumetric shrinkage ($\approx$ 1.5%) occurred during curing, with a slightly more pronounced effect in the z-direction due to the weight of the structure. This discrepancy makes CAD comparison between the nominal and recontructed models difficult, as even accounting for shrinkage a full alignment of the sections could not be performed. This occurs because during printing the structure is "self-correcting" in the sense that if the filament is not extruded in a small area due to fragmentation or bubbles the overlying layers expand slightly (as nominal layer height is lower than the filament diameter) until the surface is again leveled: this mechanism is useful for the resilience of the structure during printing, however the result is that geometry may locally shift or stretch by a small amount which is difficult to account for. As shown in Fig. 10.2.d and 10.2.e, both horizontal and vertical sections maintain the regular design structure and since the interconnected porosity and high gas permeability are preserved it appears this phenomenon does not pose significant issues to the performance of the monolith.

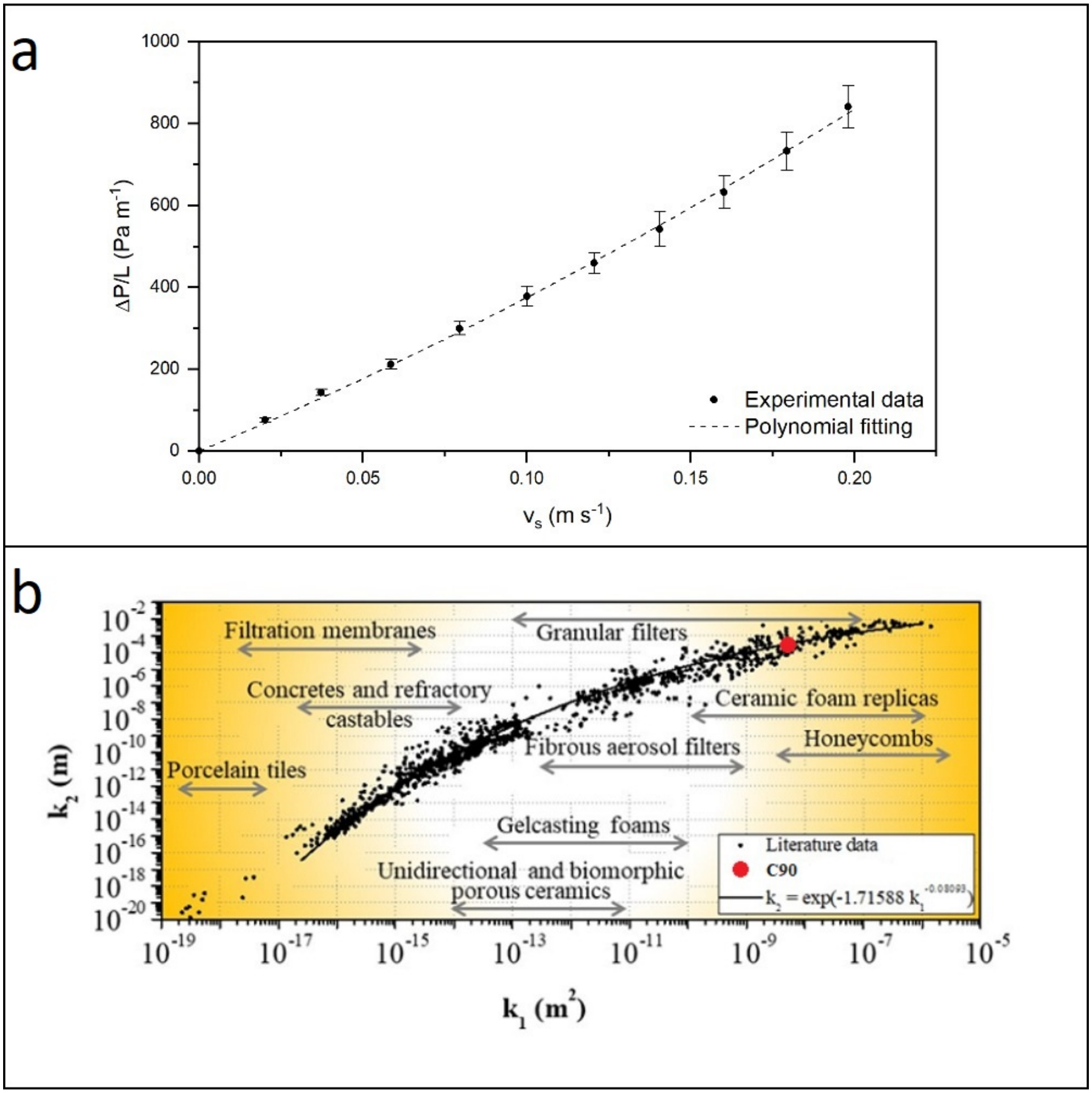

Figure 10.1: Plot of pressure drop against air velocity for showing polynomial dependence according to Forchheimer equation (a) and relative performance of C90 compared with data from literature (b).

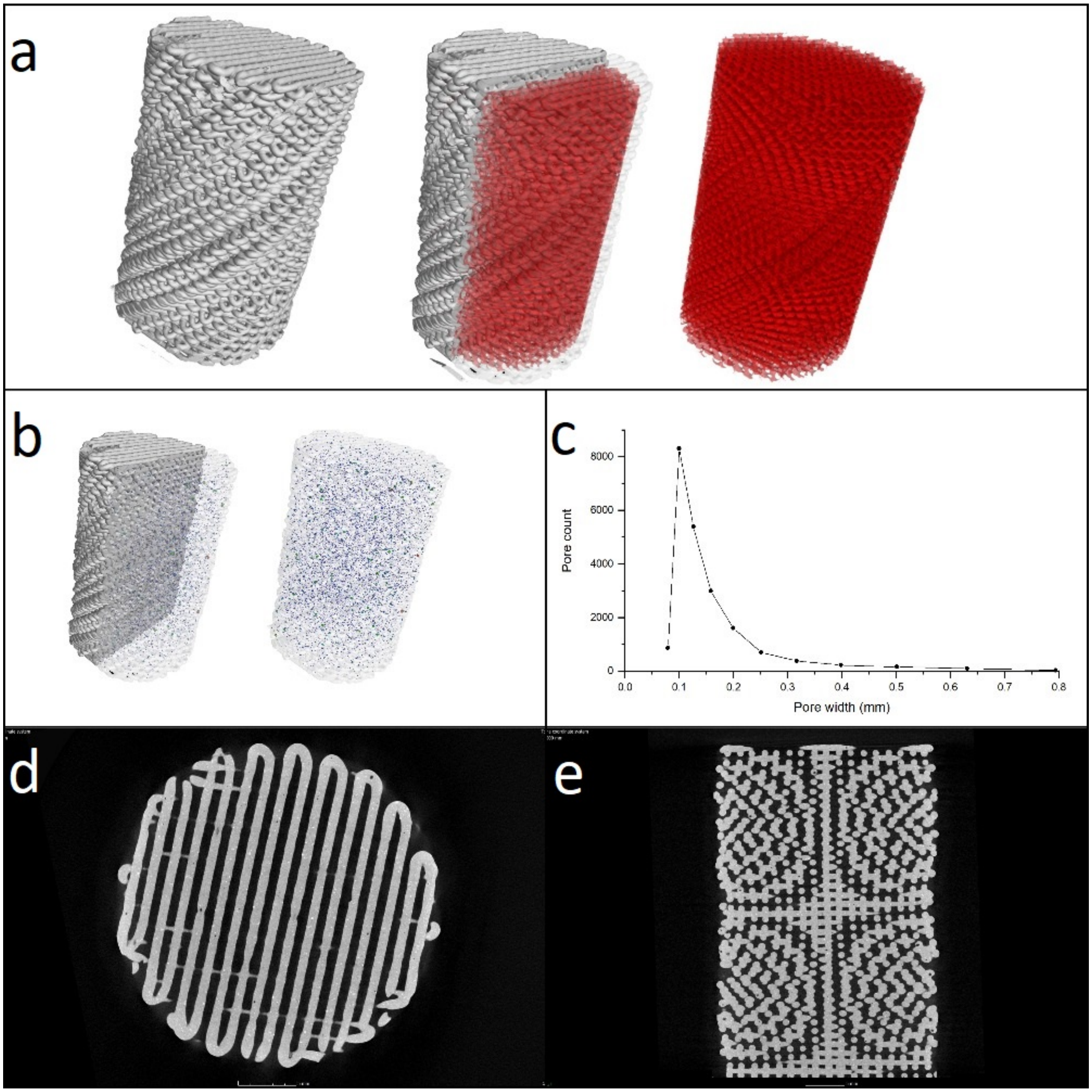

Figure 10.2: Results from micro-CT analysis of the C90 lattice: reconstructed CAD showing a single open and interconnected channel structure (a) and closed porosity from air bubbles (b), closed porosity size distribution (c) and horizontal (d) and vertical (e) sections extracted from the reconstructed CAD.

Chapter 11

Conclusions

Robocasting was evaluated for the production of hierarchically porous metakaolin geopolymer-zeolite composites for natural gas desiccation. The AM technique was shown to yield good-quality porous beam lattices with open and interconnected porosity. The use of bentonite as a binder was validated through BET measurements over PEG which yielded greatly reduced surface area compared to a reference cast geopolymer. Mechanical characterisation revealed that the addition of zeolites to a geopolymer matrix resulted in a reduction of compressive strength and Weibull modulus, however the monoliths maintained good properties which allow for safe handling and transportation. A different matrix based on sodium aluminate and colloidal silica was successfully printed using only a zeolitic filler as thickening agent and resulting in secondary crystallisation of zeolites during curing up to a cristallynity of 70%, however BET analysis revealed the surface area to be especially low ($\approx$2 m^2 g^{-1}); such phenomenon may be explained by the presence of a greatly reduced mesopore system compared to MK-based geopolymers. For the MK-based composites zeolite addition successfully increased the specific surface area of the matrix from $\approx$11 m^2 g^{-1} to $\approx$100 m^2 g^{-1} even with a relatively low filler content ($\approx$16%), with zeolite X being the most effective ($\approx$130 m^2 g^{-1}); moreover this zeolite exhibited strong water adsorption through analysis of TGA curves which makes it appropriate for the application considered. A lattice design with tortuous channels was proposed as a proof-of-concept, and successively validated by means of X-ray microtomography, which showed total interconnectivity of the design porosity, and air permeability measurements where the geometry's performance was determined to be between those of granular filters and honeycomb structures.

Appendix A

Supplementary tables: raw Weibull data

Table A.1: Fracture stresses and Weibull parameters for GP-MFI compression specimens.

j	σ_R **(MPa)**	**m (g)**	**Vt (cm^3)**	**S**	**ln(σ_R)**	**ln(ln(1/S))**
1	3.84	1.9402	0.924	0.9728	1.344517	-3.59008
2	4.58	1.9512	0.930	0.9177	1.522023	-2.45487
3	5.07	1.9375	0.923	0.8634	1.623143	-1.91845
4	5.24	1.9538	0.931	0.8069	1.656038	-1.53903
5	5.39	2.0713	0.987	0.7383	1.684244	-1.19256
6	5.60	2.1570	1.028	0.6692	1.722655	-0.91207
7	5.61	1.9929	0.950	0.6329	1.723984	-0.78196
8	5.70	2.2037	1.050	0.5428	1.739784	-0.49268
9	5.94	1.9345	0.922	0.5279	1.781815	-0.44807
10	5.98	1.8174	0.866	0.4923	1.789078	-0.34451
11	6.01	1.7552	0.836	0.4475	1.792611	-0.21817
12	6.11	2.0400	0.972	0.3339	1.810721	0.092407
13	6.75	2.0197	0.962	0.2783	1.909643	0.246077
14	7.24	2.1802	1.039	0.1937	1.979386	0.495725
15	7.76	1.9077	0.909	0.1751	2.048473	0.555218
16	7.89	1.9277	0.918	0.1076	2.066185	0.80189
17	8.74	2.2690	1.081	0.0221	2.167703	1.338204

Table A.2: Fracture stresses and Weibull parameters for GP-CHA compression specimens.

j	σ_R **(MPa)**	**m (g)**	**Vt (cm^3)**	**S**	**ln(σ_R)**	**ln(ln(1/S))**
1	3.07	1.9020	0.883	0.9754	1.121357	-3.69375
2	3.21	2.2343	1.037	0.9137	1.167694	-2.40498
3	3.59	2.2695	1.054	0.8542	1.278094	-1.84787
4	3.69	2.1158	0.982	0.8086	1.304759	-1.5492
5	3.99	2.0325	0.944	0.7622	1.383546	-1.30382
6	4.07	2.2910	1.064	0.6785	1.404863	-0.94704
7	4.12	1.8170	0.844	0.6852	1.416482	-0.97291
8	4.28	2.3547	1.093	0.5547	1.452936	-0.52882
9	4.50	2.3176	1.076	0.5027	1.503814	-0.37438
10	4.57	2.4662	1.145	0.4235	1.518441	-0.15178
11	4.59	2.2324	1.037	0.4035	1.523178	-0.09711
12	4.78	2.2238	1.033	0.3493	1.564717	0.050429
13	4.99	2.0015	0.929	0.3323	1.607843	0.096979
14	5.06	2.1588	1.002	0.2492	1.621159	0.328999
15	5.44	2.3645	1.098	0.1656	1.693607	0.586616
16	5.50	2.1419	0.995	0.1404	1.704945	0.674609
17	5.74	2.3849	1.107	0.0638	1.747382	1.012205
18	6.16	2.3500	1.091	0.0200	1.81814	1.363573

Table A.3: Fracture stresses and Weibull parameters for GP-FAU compression specimens.

j	σ_R **(MPa)**	**m (g)**	**Vt (cm^3)**	**S**	**ln(σ_R)**	**ln(ln(1/S))**
1	2.73	1.7357	0.827	0.9756	1.00404	-3.70082
2	2.83	1.8024	0.859	0.9237	1.041713	-2.53356
3	2.87	1.9224	0.917	0.8643	1.053961	-1.92563
4	2.94	2.0039	0.955	0.8023	1.077168	-1.51306
5	3.30	1.9356	0.923	0.7530	1.194101	-1.25967
6	3.37	1.9109	0.911	0.7004	1.215784	-1.03257
7	3.56	1.8345	0.875	0.6561	1.269774	-0.86413
8	4.03	2.1519	1.026	0.5505	1.394153	-0.51583
9	4.07	2.1137	1.008	0.4973	1.402779	-0.35883
10	4.59	1.9737	0.941	0.4630	1.523421	-0.26136
11	4.67	2.1066	1.004	0.3808	1.541741	-0.03504
12	4.96	1.8972	0.904	0.3603	1.602334	0.02048
13	5.36	2.2716	1.083	0.2371	1.678271	0.364255
14	5.72	1.9986	0.953	0.2218	1.743624	0.409399
15	5.75	2.2292	1.063	0.1304	1.74928	0.711606
16	6.45	2.3021	1.098	0.0696	1.864312	0.980028
17	6.81	2.2305	1.063	0.0235	1.918867	1.321734

Table A.4: Fracture stresses and Weibull parameters for GP-LTA compression specimens.

j	σ_R **(MPa)**	**m (g)**	**Vt (cm^3)**	**S**	**ln(σ_R)**	**ln(ln(1/S))**
1	3.77	1.8067	0.864	0.9639	1.327032	-3.30251
2	4.14	2.2073	1.056	0.8685	1.420568	-1.95881
3	4.38	2.2156	1.060	0.7806	1.477664	-1.39572
4	4.98	2.3978	1.147	0.6733	1.605578	-0.92729
5	5.15	2.1800	1.043	0.6125	1.639138	-0.71285
6	5.69	2.3948	1.146	0.4953	1.738928	-0.35308
7	5.84	2.4726	1.183	0.3973	1.765582	-0.08015
8	5.95	2.4250	1.160	0.3204	1.784024	0.129311
9	6.18	2.2840	1.093	0.2601	1.821846	0.29752
10	6.75	2.1446	1.026	0.2000	1.90915	0.475983
11	6.84	2.4477	1.171	0.0876	1.922359	0.890084
12	7.89	2.3510	1.125	0.0280	2.065448	1.273946

Table A.5: Fracture stresses and Weibull parameters for GP13 compression specimens.

j	σ_R **(MPa)**	**m (g)**	**Vt (cm^3)**	**S**	**ln(σ_R)**	**ln(ln(1/S))**
1	6.39	1.5401	0.694	0.9650	1.854452	-3.33606
2	6.87	1.6219	0.730	0.8881	1.927355	-2.13107
3	7.31	1.7875	0.805	0.7933	1.989774	-1.46279
4	7.87	1.5971	0.719	0.7336	2.063119	-1.17167
5	8.52	1.9091	0.860	0.5981	2.141909	-0.66552
6	9.09	1.7448	0.786	0.5339	2.207013	-0.46608
7	9.39	1.7168	0.773	0.4441	2.239177	-0.20863
8	9.77	1.7461	0.786	0.3362	2.279264	0.086309
9	10.02	2.0403	0.919	0.1750	2.304878	0.555724
10	12.71	1.9477	0.877	0.0722	2.542728	0.966128

Bibliography

[1] C. Baerlocher, L. B. McCusker, and D. Olson. *Atlas of Zeolite Framework Types*. Elsevier Science, 2007.

[2] C. Bai, G. Franchin, H. Elsayed, A. Zaggia, L. Conte, H. Li, and P. Colombo. High-porosity geopolymer foams with tailored porosity for thermal insulation and wastewater treatment. *Journal of Materials Research*, 32(17):3251–3259, Apr. 2017.

[3] A. E. Baumann, D. A. Burns, B. Liu, and V. S. Thoi. Metal-organic framework functionalization and design strategies for advanced electrochemical energy storage devices. *Communications Chemistry*, 2(1), July 2019.

[4] Y. Bouizi, I. Diaz, L. Rouleau, and V. P. Valtchev. Core-shell zeolite microcomposites. *Advanced Functional Materials*, 15(12):1955–1960, Dec. 2005.

[5] S. Brunauer, L. S. Deming, W. E. Deming, and E. Teller. On a theory of the van der waals adsorption of gases. *Journal of the American Chemical Society*, 62(7):1723–1732, July 1940.

[6] M. Calligaris, G. Nardin, and L. Randaccio. Cation site location in hydrated chabazites. crystal structure of potassium- and silver- exchanged chabazites. *Zeolites*, 3(3):205–208, July 1983.

[7] S. Chen, W. Zhang, L. P. Sorge, and D.-K. Seo. Exploratory synthesis of low-silica nanozeolites through geopolymer chemistry. *Crystal Growth & Design*, 19(2):1167–1171, Jan. 2019.

[8] R. P. Chhabra and J. Richardson. *Non-Newtonian Flow: Fundamentals and Engineering Applications*. Butterworth-Heinemann, 1999.

[9] S. Couck, J. Lefevere, S. Mullens, L. Protasova, V. Meynen, G. Desmet, G. V. Baron, and J. F. Denayer. CO 2 , CH 4 and n 2 separation with a 3dfd-printed ZSM-5 monolith. *Chemical Engineering Journal*, 308:719–726, Jan. 2017.

[10] J. Davidovits. *Geopolymer Chemistry and Applications, 3rd Ed.* Geopolymer Institute, 2011.

[11] P. Duxson, A. Fernández-Jiménez, J. L. Provis, G. C. Lukey, A. Palomo, and J. S. J. van Deventer. Geopolymer technology: the current state of the art. *Journal of Materials Science*, 42(9):2917–2933, Dec. 2006.

[12] A. Dyer. *An introduction to zeolite molecular sieves*. J. Wiley, 1988.

[13] Z. Emdadi, N. Asim, M. Yarmo, and R. Shamsudin. Investigation of more environmental friendly materials for passive cooling application based on geopolymer. *APCBEE Procedia*, 10:69–73, 2014.

[14] A. Erić, D. Dakić, S. Nemoda, M. Komatina, and B. Repić. Experimental method for determining forchheimer equation coefficients related to flow of air through the bales of soy straw. *International Journal of Heat and Mass Transfer*, 54(19-20):4300–4306, Sept. 2011.

[15] A. Fariza, A. Zuraida, and I. Sopyan. Application of low cost polyurethane (PU) foam for fabricating porous tri-calcium phosphate (TCP). *Journal of Biomimetics, Biomaterials and Tissue Engineering*, 8:1–7, Nov. 2010.

[16] S. Fasolin, M. Romano, S. Boldrini, A. Ferrario, M. Fabrizio, L. Armelao, and S. Barison. Single-step process to produce alumina supported hydroxy-sodalite zeolite membranes. *Journal of Materials Science*, 54(3):2049–2058, Sept. 2018.

[17] T. Fukasawa, M. Ando, T. Ohji, and S. Kanzaki. Synthesis of porous ceramics with complex pore structure by freeze-dry processing. *Journal of the American Ceramic Society*, 84(1):230–232, Jan. 2001.

[18] J. Grand, H. Awala, and S. Mintova. Mechanism of zeolites crystal growth: new findings and open questions. *CrystEngComm*, 18(5):650–664, 2016.

[19] S. Kulprathipanja, editor. *Zeolites in Industrial Separation and Catalysis*. Wiley-VCH, 2010.

[20] J. A. Lewis, J. E. Smay, J. Stuecker, and J. Cesarano. Direct ink writing of three-dimensional ceramic structures. *Journal of the American Ceramic Society*, 89(12):3599–3609, Dec. 2006.

[21] M. Maldonado, M. D. Oleksiak, S. Chinta, and J. D. Rimer. Controlling crystal polymorphism in organic-free synthesis of na-zeolites. *Journal of the American Chemical Society*, 135(7):2641–2652, Jan. 2013.

[22] M. L. Mcglashan. Manual of symbols and terminology for physicochemical quantities and units, Feb. 2016.

[23] MD Foster and MMJ Treacy. A database of hypothetical zeolite structures. [Online: http://www.hypotheticalzeolites.net; accessed 1-October-2019].

[24] A. Milan. *Infiltrazione di geopolimeri nel legno: uno studio sperimentale*. Università degli Studi di Padova, 2018.

[25] J. T. Muth, P. G. Dixon, L. Woish, L. J. Gibson, and J. A. Lewis. Architected cellular ceramics with tailored stiffness via direct foam writing. *Proceedings of the National Academy of Sciences*, 114(8):1832–1837, Feb. 2017.

[26] T. D. Ngo, A. Kashani, G. Imbalzano, K. T. Nguyen, and D. Hui. Additive manufacturing (3d printing): A review of materials, methods, applications and challenges. *Composites Part B: Engineering*, 143:172–196, June 2018.

[27] D. A. Nield and A. Bejan. *Convection in Porous Media*. Springer, 2017.

[28] P. L. Ph.D. and G.-F. Chen. *Porous Materials: Processing and Applications*. Butterworth-Heinemann, 2014.

[29] J. L. Provis, G. C. Lukey, and J. S. J. van Deventer. Do geopolymers actually contain nanocrystalline zeolites? a reexamination of existing results. *Chemistry of Materials*, 17(12):3075–3085, June 2005.

[30] J. L. Provis and J. S. J. van Deventer, editors. *Geopolymers: Structures, Processing, Properties and Industrial Applications (Woodhead Publishing Series in Civil and Structural Engineering)*. Woodhead Publishing, 2009.

[31] S. Rahmati. Direct rapid tooling. In *Comprehensive Materials Processing*, pages 303–344. Elsevier, 2014.

[32] O. Santoliquido, G. Bianchi, and A. Ortona. Additive manufacturing of complex ceramic architectures. In *Industrializing Additive Manufacturing - Proceedings of Additive Manufacturing in Products and Applications - AMPA2017*, pages 117–123. Springer International Publishing, Sept. 2017.

[33] P. Sazama, O. Bortnovsky, J. Dědeček, Z. Tvarůžková, and Z. Sobalík. Geopolymer based catalysts—new group of catalytic materials. *Catalysis Today*, 164(1):92–99, Apr. 2011.

[34] J. Schmidt, H. Elsayed, E. Bernardo, and P. Colombo. Digital light processing of wollastonite-diopside glass-ceramic complex structures. *Journal of the European Ceramic Society*, 38(13):4580–4584, Oct. 2018.

[35] K. S. W. Sing. Reporting physisorption data for gas/solid systems with special reference to the determination of surface area and porosity (recommendations 1984). *Pure and Applied Chemistry*, 57(4):603–619, Jan. 1985.

[36] S. SOLLER, V. KAUFMANN, and F. LAITHIER. Design and testing of liquid propellant injectors for additive manufacturing. 2017.

[37] J. D. Sullivan and P. H. Lauzon. Experimental probability estimators for weibull plots. *Journal of Materials Science Letters*, 5(12):1245–1247, Dec. 1986.

[38] M. M. J. Treacy and J. B. Higgins. *Collection of Simulated XRD Powder Patterns for Zeolites Fifth (5th) Revised Edition*. Elsevier Science, 2007.

[39] X.-Y. Yang, L.-H. Chen, Y. Li, J. C. Rooke, C. Sanchez, and B.-L. Su. Hierarchically porous materials: synthesis strategies and structure design. *Chemical Society Reviews*, 46(2):481–558, 2017.

[40] Zeolite-Italia. *Italian Chabazite: data sheet*, 12 2018.

[41] J. Zha, X. Yin, J. R. Baltzegar, and X. Zhang. Coordinatively unsaturated metal site-promoted selective adsorption of organic molecules on supported metal–organic framework nanosheets. *Langmuir*, Sept. 2019.

Ringraziamenti

Chi mi conosce sa che non sono bravo con questo tipo di situazioni, ma eccoci qua.

Innanzitutto vorrei ringraziare i miei relatori, l'Ing. Giorgia Franchin e il Prof. Paolo Colombo, per l'enorme supporto che mi hanno dato e l'incrollabile entusiasmo che mi hanno saputo trasmettere nel corso di questi otto mesi. Un sentito ringraziamento anche alla Dott.ssa Renata Fuss Botti, che mi ha seguito fin con troppa pazienza, e a tutto il Laboratorio dove ho trovato un ambiente rilassato e accogliente con persone sempre disponibili.

Ovviamente non posso evitare di ringraziare mia madre, mio padre, mio fratello e tutto il resto della mia famiglia che mi hanno sempre sostenuto pienamente nella buona e nella cattiva sorte. Sarei perso senza di voi, e non ve lo dico abbastanza.

Un sentito ringraziamento all'Ing. Alessandro Pace e a Airlife, senza di cui questo progetto non sarebbe stato possibile, e alla Dott.ssa Sara Carturan, il Prof. Simone Carmignato e il Prof. Murilo Innocentini per le analisi che hanno eseguito sui miei campioni.

E infine, ma sono sicuro che non se la prenderanno, non mi resta che ringraziare i miei amici. Sono diec'anni che vi vedo più della mia famiglia, e vi amo ancora come il primo giorno.